

TGF- β associated senescence and impaired metabolism in central memory CD4 T cells promotes HIV persistence

Rafick Sekaly (✉ rafick.sekaly@emory.edu)

Emory University

Khader Ghneim

Emory University

Ashish Sharma

Emory University

Susan Ribeiro

Case Western Reserve University

Slim Fourati

Case Western Reserve University <https://orcid.org/0000-0001-6609-7587>

Jeffery Ahlers

Calimmune

Deanna Kulpa

Department of Pediatrics, Emory University School of Medicine, Atlanta, GA. <https://orcid.org/0000-0002-0411-7295>

Xuan Xu

Case Western Reserve University

Jessica Brehm

ViiV Healthcare

Aarthi Talla

Allen Institute for Immunology

Benigno Rodriguez

Case Western Reserve University

Carey Shive

Case Western Reserve University

Razvan Cristescu

MERCK <https://orcid.org/0000-0002-9978-0339>

Andrey Loboda

Merck & Co., Inc. <https://orcid.org/0000-0003-4239-184X>

Robert Balderas

BD Biosciences <https://orcid.org/0000-0002-8734-8629>

I-ming Wang

Pfizer

Peter Hunt

University of California

Daniel Lamarre

University of Montreal

Daniel Douek

NIH

Daria Hazuda

Merck Research Laboratories

Michael Lederman

Case Western Reserve University

Steven Deeks

University of California, San Francisco <https://orcid.org/0000-0001-6371-747X>

Article

Keywords: HIV, CD4 T-cell reconstitution, cellular senescence

Posted Date: September 28th, 2021

DOI: <https://doi.org/10.21203/rs.3.rs-923015/v1>

License: © ⓘ This work is licensed under a Creative Commons Attribution 4.0 International License. [Read Full License](#)

Abstract

Current therapeutic interventions to eradicate latent HIV (“reservoir”) and restore immune function in ART-treated HIV infection have yet to show efficacy. To explore mechanisms of HIV persistence, we apply an integrated systems biology approach and identify a distinct group of individuals with poor CD4 T-cell reconstitution (Immunologic non-responders, “INRs”) and high frequencies of cells with inducible HIV. Contrary to the prevailing notion that immune activation drives HIV persistence and immune dysfunction, peripheral blood leukocytes from these subjects have enhanced expression of a network of genes regulated by cellular senescence. In these subjects, increased frequencies of regulatory T cells and expression of the TGF- β signaling cascade are concomitant with the downregulation of cell cycle and metabolism in CD4 central memory T (TCM) cells. These cascades, downstream of TGF- β , lead to the accumulation of PD-1 expressing CD4 TCM and are associated with an increase in frequencies of cells with inducible HIV ex vivo. In vitro validation confirmed that this cellular profile was driven by a β -hydroxybutyrate/bile acid rich metabolic milieu and resulted in TGF- β associated latency establishment. Our findings identify targets for PD-1 or TGF- β specific interventions that can overcome cellular senescence; these therapeutic approaches have shown safety and efficacy in cancer, and may prove to be crucial for HIV eradication.

Introduction

HIV infection remains a major global public health concern (WHO, <https://www.who.int/news-room/fact-sheets/detail/hiv-aids>). Although effective combined anti-retroviral therapy (cART) has altered the course of HIV disease by preventing viral replication, it is not curative and does not fully restore immune function¹. Depending on the population studied and outcome definitions², up to 20% of cART-treated subjects fail to reconstitute CD4 + T-cell numbers despite years of effective treatment with sustained HIV suppression, and are predisposed to excessive risk of non-HIV comorbidities³.

These immune non-responder subjects (INRs) show severe homeostatic alterations in CD4 T-cells, including lower frequencies of naïve CD4 T-cells, accumulation of highly differentiated T-cells, T-cell activation and apoptosis⁴⁻⁶. Furthermore, these CD4 T cells express makers of replicative senescence⁷ and exhaustion⁸; and have increased frequencies of immunosuppressive CD4 + regulatory T-cells (Tregs)⁹. Indeed, we have previously reported that a multivariate model characterized by naïve T-cell depletion, higher frequencies of cycling CD4 + central memory (CM) and effector memory (EM) T-cells, expression of the T-cell activation markers (CD38, HLA-DR, CCR5 and/or PD-1 ($p < 0.0001$)), and levels of soluble CD14 (sCD14) can distinguish INRs from immune responder subjects (IRs), even after adjustments for key clinical indices like CD4 + T-cell nadir and age at cART initiation¹⁰⁻¹². On the immunological front, studies have shown that impairment in IL-7/L-7R signal transduction axis¹³, chronic inflammation and persistent type I interferon production could mediate poor CD4 T cell homeostasis, reduced thymic function¹⁴. In addition, changes in metabolic milieu (i.e. increase in SCFAs or bile acids) that induce Treg differentiation/impair effector CD4 T cell function can also drive poor immune reconstitution in INRs¹⁵⁻¹⁷.

The aforementioned alternations in CD4 T cell homeostasis are further complicated by the fact that pro-viral HIV DNA integrates into the human genome and persists within memory CD4 T-cells¹⁸. This cellular “reservoir”

reignites rounds of virus replication if cART is interrupted¹⁹, stressing the need for long-term cART administration. While, reconstitution of CD4 counts during uninterrupted cART leads to a decrease in intact proviral DNA²⁰, elevated levels of inflammatory markers characteristic of INRs (IL6, TNF α , IL1 β , IFN α/β , MIP1 α/β , RANTES) are associated with HIV persistence²¹. HIV replication triggered by this inflammation can alter homeostatic proliferation and sustain the HIV reservoir by occasional expansion and contraction of individual CD4 T-cell clones²²⁻²⁴. Indeed, increased expression of co-inhibitory receptors (PD-1, LAG-3, and TIGIT) that can drive cellular quiescence upon receptor engagement and inhibit HIV replication, have been shown to contribute to the magnitude of the HIV reservoir²⁴⁻²⁶. Here, we studied two independent cohorts of HIV-infected cART-treated individuals and identified INRs with a senescent CD4 T cell profile that was observed to be downstream of α -ketobutyrate induced differentiation of TGF- β producing Tregs. CD4 T cells from these INR subjects showed reduced homeostatic proliferation (leading to lack of CD4 recovery), and heightened frequencies of inducible HIV RNA.

Results

We used an unbiased approach that integrates datasets from peripheral blood transcriptome, high density flow cytometry and plasma cytokine measures to identify cellular and molecular drivers of HIV persistence and lack of CD4 T cell recovery (Supplementary Fig. 1a), in two independent cohorts of HIV-infected subjects (see Study Participants in Material and Methods; Table S1, Table S2). All subjects were under cART for at least three years and maintained consistently low CD4 T cell counts up to four years prior to sample collection (Supplementary Fig. 1b). The Cleveland Immune Failure cohort (CLIF) was comprised of 61 subjects (17 immune responders - IRs - >500 CD4 T-cells/mm³ and 44 immune non-responders - INRs - <350 CD4 T-cells/mm³); whereas, the Study of the Consequences of the Protease Inhibitor Era cohort (SCOPE) included 41 subjects (20 IRs with >500 CD4 T-cells/mm³ and 21 INRs with <350 CD4 T-cells/mm³).

Transcriptional profiling reveals systemic senescence as a driver of poor immune reconstitution

Exploratory analyses of whole blood transcriptomic data (CLIF cohort subjects; using unsupervised clustering described in the methods) (Fig. 1a and Supplementary Fig. 1c) identified three groups of subjects with unique transcriptional profiles: IRs and two distinct INR groups, "INR-A" and "INR-B". INR-As exhibited the highest transcriptomic variation from IRs with approximately 3000 differentially expressed genes (DEGs). In contrast, INR-Bs were proximal to IRs with <400 DEGs (Table S3-5). Age, years on cART, CD4 T cell counts, CD4 T cell nadir, markers of gut barrier dysfunction (sCD14), and inflammation (IL-6, IP10) - known predictors of morbidity and mortality in INRs²⁷ - failed to distinguish the two INR groups (Supplementary Fig. 1d-p). Interestingly, DEGs specific to INR-As were mostly down-regulated (72% and 66% when contrasted against IRs and INR-Bs, respectively), suggesting a quiescent transcriptional state in these subjects (Supplementary Fig. 2a).

Comprehensive pathway analyses using MSigDb's Hallmark module²⁸⁻³⁰ (Fig. 1b, Table S6) revealed that a majority of the pathways, likely driven by significantly elevated CD4 T cell numbers, were upregulated in IRs when compared to both INR-As and INR-Bs. Notably, when contrasting INR-As against INR-Bs (where CD4 T cell numbers are comparable), INR-As were observed to have significantly decreased expression of inflammation,

cell cycling, apoptosis, metabolism genesets^{31,32}. This transcriptional profile was in line with reduced expression of genes regulated by Myc (a primordial transcription factor (TF) that regulates proliferation and metabolism of activated T cells)³³ and was indicative of a senescent state^{31,32}.

Cell subset deconvolution (using gene signatures from Nakaya et al³⁴) showed that genesets specific to all major innate and adaptive immune cell subsets were reduced in INR-As (vs INR-Bs) (Fig. 1c, Table S7). Similarly, down-regulation of gene signatures for specific CD4 and CD8 T-cell subsets (naive, memory and effector cell, extracted from Novershtern et al³⁵ - see methods for detail) were also observed (Fig. 1d, Table S8). The down-regulated signatures in T-cells, myeloid dendritic cells (mDCs) and monocytes mapped to genes that drive apoptosis, transcription/cell migration, and cellular/lipid metabolism (lipid storage, GTP metabolic process), respectively (Supplementary Fig. 2b). These data provide evidence for decreased global transcription and systemic senescence in immune cells from INR-As, when compared to INR-Bs or IRs.

Transcriptional profiles downstream of FOXO3 and SMAD2/3 signaling are enriched in senescent INRs

To identify mechanisms underlying poor immune reconstitution observed in INR-As, we identified TFs ($p < 0.05$, Supplementary Fig. 2c, Table S9) and mapped the pathways that were associated with genes upregulated (Reactome pathway database, ClueGO plugin in Cytoscape, $FDR < 0.05$)^{36,37} in the INR-As (vs IRs and INR-Bs; $FDR < 0.05$, Table S10). The upregulated TFs included IRF3 (driver of type I IFN production³⁸), FOXO3 (transcriptional repressor³⁹), SMAD2 (TGF- β signaling⁴⁰) and CCNT2 (Negative regulator of HIV Tat protein; i.e. driver of HIV latency induction⁴¹) (Supplementary Fig. 2c). Interestingly, enrichment of cellular processes downstream of these TFs - including heme metabolism, TGF- β signaling, IRF3 activation, reactive oxygen species (ROS) production and inhibition of NF- κ B activation (Fig. 1e) - were observed in these subjects. Specifically, INR-As showed increased expression of features of senescence that included FOXO3 regulated genes like SOD/CAT⁴²⁻⁴⁴ (driver of ROS production) (Fig. 1e); FOXO4/TP53⁴⁵ driven anti-apoptotic genes (BCL2L1; $FDR < 0.01$)⁴⁶⁻⁴⁸ (Table S5); and targets of SMAD2/3 including 'Inducer of Promyelocytic Leukemia' (PML; conductor of TGF- β signaling via SMAD2/3, and regulator of HIV latency^{49,50}), WEE1⁵¹ (cell cycle regulator) and GLUL^{52,53} (metabolic regulator). The downregulation MYC target genes (known to control ribosomal biosynthesis and translation)⁵⁴, genes of the electron transport chain, and genes regulating major metabolic pathways (including glycolysis, oxidative phosphorylation and fatty acid metabolism) further confirmed the senescent nature of these subjects (Supplementary Fig. 2d, Fig. 1b). The senescent/anti-inflammatory profile of INR-As contrasted the pro-inflammatory profile of INR-Bs where the enrichment of pathways downstream of TLR/IL1, cell cycling, and apoptosis/pyroptosis was observed. Increased expression of several members of the pro-inflammatory NF- κ B family of TFs (NFKB1, NFKB2 and RELB), upregulation of NF- κ B target genes including chemokines (e.g. CCL2 and CCL17)⁵⁵, genes of the inflammasome complex (NLRP3, IL1B and IL18)⁵⁶ and effector genes driving apoptosis/pyroptosis (e.g. CASP4, DIABLO, CASP2 and CASP3)⁵⁷ were characteristics of this group (Supplementary Fig. 2d).

Overall, our data suggest that the INR-As have increased expression of a signaling cascade downstream of TGF- β (SMAD2/3; PML) which culminates in the upregulation of FOXO3/4 driven senescence - characterized

by impaired cell metabolism and cell cycle arrest⁵⁸. INR-As will henceforth be referred to as “Senescent-INRs”.

A gene-based classifier segregates the two INR groups in whole blood and in sorted central memory CD4 T cells

Next, we built a gene-based nearest shrunken centroid classifier (see methods) to identify Senescent-INRs in other cohorts of HIV infected cART treated subjects. The 352 features (genes, Table S11) classifier was trained on the CLIF cohort and had a misclassification error rate of 0.26 (Fig. 1f). To validate the capacity of the classifier to differentiate immune cell subsets from Senescent INRs (vs INR-Bs), we tested the enrichment of the classifier geneset in sorted CD4 TCM, CD4 TEM (effector memory T cells) and innate immune (HLA-DR+CD19-) cells. We observed that unlike the CD4 TEM and innate subsets, the classifier geneset was enriched in the CD4 TCMs from the senescent INRs (Fig. 1g). In line with the whole blood signatures (Fig. 1b), metabolic, cell cycling and apoptosis pathways were significantly reduced in these CD4 TCMs. Whereas, pathways that define quiescence (WNT/b-catenin signaling pathway) and senescence (cellular/oxidative stress induced) were enriched in CD4 TCMs from senescent INRs (Fig. 1h). Overall, these observations suggest that CD4 TCMs from the senescent INRs are metabolically impaired, have poor cell cycling capacity and could serve as hubs that maintain high levels of HIV reservoir.

Classifier confirms the generalizability of the Senescent-INR phenotype in HIV-infected subjects

Using an unsupervised approach (initially applied in the CLIF cohort), we confirmed two distinct INR groups in the SCOPE cohort (Supplementary Fig. 3a, Supplementary Fig. 3b). The 352-gene classifier segregated these two INR groups in the SCOPE cohort with an accuracy of 81% (Fig. 2a) - validating the generalizability and reproducibility of two INR groups (Fig. 2b: PCA representation of the 352-gene classifier across the SCOPE cohort) and highlighting the potential use of this classifier to distinguish Senescent-INRs in clinical settings. Our classifier (Table S11) included genes that drive a senescent biology (FOXO3, FOXO4, TGFBR2, RIOK3, IRF3 and BCL2L1)^{46,59,60,61} and regulators of mitochondrial activity (NDUFS3, CYB5R3, ATP5G2)⁶². Several transporters of macromolecules: SLC6A8 (Sodium- and chloride-dependent creatine transporter¹⁶³), SLC48A1 (Heme transporter⁶⁴), SLC4A1 (Band 3 anion transporter⁶⁵), SLC25A23 (Mitochondrial Calcium carrier⁶⁶) and SLC38A5 (glucose⁶⁷) upregulated in Senescent-INRs and were also features of the classifier (Table S11). Overall, we observed that molecular pathways specific to cellular senescence⁶⁸⁻⁷¹ discriminate the two INR groups and counter-intuitively suggest that failure to increase CD4 T-cell numbers in senescent could be due to senescence and not to previously described pro-inflammatory cascades¹⁰.

The classifier gene set highlights the role of senescence in driving the magnitude of the inducible HIV reservoir

Although poor immune reconstitution has been associated with HIV persistence⁷², the cellular effectors and molecular mechanisms driving this association remain unidentified. To assess the role of senescence in HIV

persistence, we measured frequencies of CD4 T-cells with inducible multi-spliced HIV RNA (“inducible HIV”) - in all subjects from the SCOPE cohort - using the Tat/rev Induced Limiting Dilution Assay (TILDA)⁷³. Our data show that Senescent-INRs have significantly higher inducible HIV when compared to IRs (~4.3-fold increase in median values, $p < 0.021$) and INR-Bs (~5.5-fold increase in median values, $p = 0.046$) (Fig. 2c). And, these Senescent-INR subjects with the highest levels of inducible HIV were significantly enriched in (i.e. could be predicted by) the classifier geneset (Fig. 2d). Interestingly, inducible HIV levels in Senescent-INRs were negatively correlated with CD4 counts ($\rho = -0.52$; $p < 0.05$; while this correlation was not significant in inflammatory INRs and in IRs). Comprehensive pathway analyses of the whole transcriptome further confirmed that genesets characteristic of Senescent-INRs (i.e. cell cycle arrest and ROS production) were associated with higher inducible HIV (Table S12).

Increased frequencies of TGF- β producing Tregs and PD1+ TCMs with impaired metabolism drive lower CD4 counts and HIV persistence

Given that transcriptional profiling identified the TGF- β pathway (PML, SMAD2/3; Fig. 1e, Supplementary Fig. 2 c,d) as a driver of cellular senescence in our cohort and that Forkhead box P3 (FOXP3) expressing T-regulatory cells (Tregs) are a primary source of TGF- β ^{74,75}, we sought to ascertain the role of Tregs in driving senescence and HIV persistence. To this end, we developed a high-dimensional flow cytometry panel (Table S13) to quantify master regulators of Treg function (SATB1 and FOXP3⁷⁶), to discriminate differentiated Tregs (CD45RA, CD49B and CD39⁷⁷), to assess proliferation (Ki67) and TGF- β activation potential of a CD4 T cell (expression of latent (LAP) or activated (GARP) forms of TGF- β ^{78,79}). UMAP dimension reduction (<https://arxiv.org/abs/1802.03426>) (Fig. 3a). followed by unbiased clustering⁸⁰ (Fig. 3a) led to the identification of three clusters of CD4 T cells (Fig. 3b, Fig. 3c, Table S14) that were enriched in senescent INRs (vs IRs) and expressed markers characteristic of TGF- β producing Tregs (FOXP3, CD25, lowCD127, LAP and GARP) (Fig. 3c). The most abundant of these clusters (i.e. Cluster 7; 0.81-5.34% of CD4 T cells) also showed an effector Treg phenotype (high CD39, low CD45RA) and low levels of markers that define IL-10 production capacity (Tr1) (i.e. CD49B, LAG3⁸¹) (Fig. 3c).

We assessed the systemic impact of these Treg clusters by studying their association with clusters of cytokines that define the host plasma milieu. We applied an unsupervised clustering using independent methods (k-means, and hierarchical clustering⁸²) to identify four clusters of plasma cytokines (from 43 cytokines tested) across all subjects of the SCOPE cohort (Supplementary Fig. 4a,b,c). Of these, the overall centroid score of “Cytokine Cluster 3” was significantly associated with the 352-gene classifier in Senescent-INRs (NES = 2.9, FDR = 0, Supplementary Fig. 4d, Table S15). No significant correlation between “Cytokine Cluster 3” centroid score and the classifier genes was observed in INR-Bs or IRs (Table S15). This cytokine cluster included several anti-inflammatory cytokines: TGF- β 1, TGF- β 2 (triggers of the TGF- β pathway⁸³), IL13 (known to inhibit inflammatory cytokine production⁸⁴), KC/GRO (CXCL1) (another anti-inflammatory cytokine⁸⁵), VEGF (the inhibitor of apoptosis⁸⁶) and homeostatic cytokines (IL3, IL7)^{87,88} (Supplementary Fig. 4c). Importantly, our data showed that frequencies of GARP+ Tregs (Treg cluster 7) were univariately correlated with members of “Cytokine Cluster 3” (Fig. 3d, including TGF- β 2 and IL-7; Table S16), and were associated with

an enrichment in the classifier genes (significantly overlapped leading edge genes represented in Fig. 3e, Table S17).

The downstream impact of heightened frequencies of TGF- β secreting Tregs on HIV latency was further confirmed by the observation that ChIP-Seq validated SMAD2/3 targets⁸⁹ and HDAC1/2 targets (induced after siRNA knockdown)⁹⁰ were more abundant in subjects with the highest inducible HIV and frequencies of GARP+ Tregs (Fig. 3e). These genesets included genes that activate latent TGF- β (i.e. FURIN⁹¹), restrict T cell differentiation (LGAL3; inducer of TGF- β driven activation of b-catenin^{92,93}), reduce cell cycling (i.e. GADD45A⁹⁴) and restrict chromatin accessibility (co-operation between HDAC1/2 targets and SMAD2/3) can to induce cell quiescence (Fig. 3e).

Increased frequencies of senescent PD1+ TCMs with impaired mitochondrial function drive lower CD4 counts in the senescent INRs

Given that signaling via TGF- β /FOXO3 axis drives surface PD1 expression⁹⁵, cell cycle arrest and impaired metabolism⁹⁶ - we used high-dimensional flow cytometry, transcriptomics and cytokine data to identify the cellular drivers of immune reconstitution or lack thereof; we hypothesized that the upregulation of surface PD-1 and reactive oxygen species (ROS; measured by intracellular CellROX staining) in CD4 T-cells could be associated with lower CD4 counts⁹⁷. Using the analytical strategy described in the section above, we identified a cluster of PD1^{hi} ROS^{hi} CD4 central memory T-cells (TCM, Cluster 9; Fig. 4a,b,c, Table S18) that was induced in Senescent-INRs when compared with IRs (but not in INR-Bs vs IRs). Conversely, a cluster of PD1^{hi} ROS^{lo} CD4 effector memory T-cells (TEM, Cluster 17; Fig. 4a,b,c, Table S18) was uniquely upregulated INR-Bs. Frequencies of PD1+ CD4/CD8 TCM cells were directly correlated with the frequencies of GARP+ Tregs (Treg cluster 7) and with cytokine cluster 3 (Fig. 4d). In line with previous studies^{24,98}, these data confirm the negative impact of PD-1 expression on T-cell homeostasis and immune reconstitution.

Evidence of impaired metabolism and cellular senescence in these PD1^{hi} ROS^{hi} TCMs was obtained by identifying metabolic and cell cycling genesets that associate with this cell subset (in senescent INRs vs IRs). Individuals with higher levels of PD1^{hi}ROS^{hi} TCMs had poor mitochondrial metabolism profiles (higher ROS and lower oxidative phosphorylation), reduced cMyc activity and increased expression of genes that drive cellular senescence (Fig. 4f, Table S19). Specifically, expression of catalase (CAT), peroxidins (PRDXs) and cell cycle inhibitory genes (i.e. CDKN2D) was increased in senescent-INRs; while genes that regulate oxidative phosphorylation (NDUFs and COXs) and MYC target genes were expressed at lower levels. Concurrently, frequencies of PD1^{hi}ROS^{hi} TCMs were also associated with cellular senescence pathways downstream of impaired mitochondrial activity (i.e: oxidative stress induced senescence, SASP), and were observed to be the highest in subjects with higher inducible HIV (Fig. 4e, Table S19). Altogether, these results indicate that PD1 expressing TCMs with impaired mitochondrial metabolism are senescent cells lacking the capacity to cycle and to differentiate into effector cells, thereby driving low CD4 cellular counts.

Bile and short chain fatty acid profiles drives Treg differentiation and TGF- β production in Senescent-INRs

The role of Tregs and impaired T cell homeostasis has been well characterized in prominent metabolic diseases (from diabetes, cancer and cardio vascular diseases)⁹⁹⁻¹⁰³. Subjects presenting such metabolic aberrations have impaired host/microbe driven metabolic profiles that impair T cell function. To understand the metabolic milieu that could regulate Treg function in senescent INRs, we performed mass spectrometry (MS) to identified plasma metabolites that would be associated (*ex vivo*) with or could trigger (*in vitro*) Treg differentiation, TGF- β production or senescence. An unbiased assessment of the plasma metabolite profile of SCOPE cohort participants revealed that one of the primary components of variation (Principal Component 1 and Principal Component 2; derived from PCA analyses of ~750 detectable metabolites) was associated with inducible HIV (PC2 vs TILDA p-value <0.05; Fig. 5a). Specifically, the metabolite that were univariately correlated (p-value<0.05) with inducible HIV levels included members of the liver-biliary axis (i.e. primary liver/bile metabolites like bilirubin, biliverdin, cholate and glycol-beta-muricholate; secondary liver/bile metabolites like ursodeoxycholate), carnitine derivatives and members of the hydroxybutyrate family (i.e. a-ketobutyrate and hydroxybutyryl carnitine) (Fig. 5b). Several, but not all, of these metabolites were also associated with SMAD2/3 and HDAC1/2 target genesets and frequencies of GARP+ Tregs (Fig. 5b). Importantly, this analysis showed that a-ketobutyrate - a correlate of inducible HIV - was also correlated with C7 GARP+ Treg frequencies (p = 0.089), emphasizing the association between Tregs, metabolome and inducible HIV. Together these data indicate that metabolites could constitute integral components of the mechanisms that fuel HIV persistence.

TGF- β production resulting from alpha-ketobutyrate driven Treg differentiation causes increased HIV latency in vitro

To establish a causal link between butyrate metabolites on GARP+ Treg differentiation, we used the approach described by Ohno and Rudensky^{17,104}. Briefly, increasing concentrations of a-ketobutyrate were added to healthy sorted naïve CD4 T-cells stimulated with IL-2, anti-CD3/28 and/or TGF- β (Fig. 5 c,d) changes in frequencies of TGF-b secreting FOXP3+ cells were monitored¹⁰⁵. We observed that, stimulation of naïve T cells with high concentrations of a-ketobutyrate (in the absence of TGF- β) preferentially led to the differentiation of naïve T-cells into GARP+FOXP3+ cells (Fig. 5 c,d) that secreted significant amounts of TGF- β 1 (Fig. 5e). Of note, a further increase in GARP+ Treg differentiation when both TGF- β and alpha-ketobutyrate were added to the culture (Supplementary Fig. 5a). Aside from Tregs, Increasing concentrations of a-ketobutyrate also led to significantly increase in PD1 expressing CD4 T-cells (Fig. 5 c,d, Supplementary Fig. 5b) that were associated with loss of effector function - shown by reduced secretion of T-helper cytokines in the culture media (i.e. IL17A, IFN- γ , IL9) (Fig. 5f). Altogether, these data indicate that in addition to enhancing Treg differentiation, the abundance of b-hydroxybutyrates could drive the upregulation of TGF- β associated suppressive activity of Tregs. The latter, as shown in Fig. 3, are critical for the maintenance of the HIV reservoir.

To provide evidence for a direct role of TGF- β in the induction of HIV latency, we developed an *in vitro* culture model¹⁰⁶ where TGF- β was added to HIV-infected CD4 T-cells. Increased numbers of CD4 T-cells with integrated proviral DNA were observed after 14 days of culture with increasing concentrations (0 to 50 ng/mL) of TGF- β

($r = 0.7$; $p = 0.009$) (Fig. 6a), demonstrating that TGF- β contributes to heightened levels of non-replicative forms of HIV DNA and establishment of HIV latency. In addition, we observed (in line with *ex vivo* observations shown in Fig. 4b) an increase in surface PD-1 levels at the two highest doses of TGF- β in the CD4 TCM subset (Fig. 6b). We then reversed latency by stimulating these CD4 T cells with immobilized CD3 and soluble CD28 specific antibodies. Our data show that frequencies of HIV p24+ cells were significantly higher in conditions where the highest concentrations of TGF- β (0.2-20ng/mL) were added (Fig. 6c). These frequencies of HIV p24+ cells were correlated with surface PD-1 levels on CD4 TCM (Fig. 6d). Altogether, these *in vitro/ex vivo* observations validate the critical role of TGF- β producing Tregs in driving the mechanistic establishment and/or maintenance of the HIV reservoir.

Integrated multi-omic model highlights cellular and molecular effectors of senescence as drivers of HIV persistence and lack of immune reconstitution

Using unbiased and holistic approaches, we have highlighted gene expression profiles, cytokines and T-cell subsets that are independently associated with HIV persistence and lack of CD4 reconstitution in the Senescent INRs. To investigate the interplay of pathways driving these cellular phenotypes and HIV persistence, we integrated multi-omic signatures above (Figures 2, 3 and 4, Table S20) across all subjects ($n=41$). Our data show that the levels of inducible HIV were positively correlated to senescence - characterized by impaired metabolism⁹⁷ (increased ROS, decreased OXPHOS), reduced transcription/translation (RPSs and EIFs) downstream of poor cMYC activity and TGF- β signaling (SMAD2/3 target genes) (Fig. 6e, Supplementary Fig. 5c). The induction of these cascades was consistent with higher expression of the transcriptional repressors that induced senescence (i.e. FOXO3, FOXO4)⁴⁵, and with lower expression of master regulators of innate antiviral activity (i.e. IRF7 and restriction factors of viral replication) (Supplementary Fig. 6). Lack of CD4 reconstitution and HIV persistence was also driven by higher frequencies of GARP+ Tregs, increased expression of SMAD2/3 targets (including FURIN, SMOX) and heightened levels of IRF3 induced genes (i.e. AFF, DARC, GUK1) (Supplementary Fig. 6). Our integrated analyses indicate that most pathways that drive HIV persistence are negatively associated with the recovery of CD4 numbers upon cART initiation in senescent subjects; and provided further evidence for the direct interplay between Treg frequencies, TGF- β production, heightened FOXO3 expression, interferon signaling, establishment of cellular senescence, impaired T cell homeostasis, and quiescent cellular and metabolic state as conditions that favor the maintenance of HIV reservoir in the unique senescent INR population described here.

Discussion

In this manuscript, we identified cellular senescence as a mechanism that underlies HIV persistence and failure to reconstitute CD4 T-cell numbers in two independent cohorts of HIV infected cART-treated subjects. Our results provide a mechanistic framework where anti-inflammatory cytokines, TGF- β , VEGF and IL-13, trigger the upregulation of a transcriptional network that drives Treg differentiation. Our integrated analysis shows that increased frequencies of TGF- β producing Tregs and metabolically impaired PD-1 + TCMs drives, senescence, HIV persistence and poor CD4 T cell reconstitution.

Senescent-INRs, in our study, show increased expression of several molecules which are features of senescent cells. These include: FOXO4, TF upstream of the induction of senescence⁴⁵; PML, triggers cellular quiescence, HIV latency and is also downstream of TGF- β ; as well as molecules with anti-apoptotic activity (BCL-2, BCL-xL¹⁰⁷) that ensure the survival of senescent cells⁷¹. In addition, FOXO3 - known to transcriptionally regulate genes involved in redox balance and anti-oxidant defenses^{108,109} – and its targets like SNCA (α -synuclein¹¹⁰), mitophagy related genes (PINK1 and PARKIN¹¹¹) and GABARAPL2 (the autophagy regulatory gene¹¹²) and SLCs were observed to be upregulated in Senescent-INRs as part of a mitochondrial damage response. The downregulated oxidative phosphorylation and glycolysis observed in these subjects could be driven by the upregulation of FOXO3 target genes CYB5R3 and peroxiredoxins (PRDX2, PRDX3, PRDX5) involved in maintaining redox balance and anti-oxidant defense¹¹³. PRDXs, specifically PRDX2, can get oxidized by ROS due to a lack of electron transport in the mitochondria¹¹³ and can activate kinases (like p38) to initiate stress responses and protect cells from ROS mediated cell death, thereby supporting the survival of senescent cells¹¹³. In our data, the expression of genes associated with ROS production (Catalase and superoxide dismutase) and oxidized lipid biogenesis (CD36) were positively correlated with HIV reservoir size and confirm the link between senescence and HIV reservoir establishment.

The aforementioned senescence associated impaired mitochondrial metabolism in the senescent-INRs was also found to be associated with increased frequencies of PD-1 + TCMs and is suggestive of an accumulation of these cells in an early memory differentiated state. Indeed, we and others have shown that PD-1 expression leads to the accumulation of cells in an early memory differentiated stage¹¹⁴ while the genetic ablation of PD-1 results in increased differentiation to the effector memory stage¹¹⁵. Additionally, T-cells from Senescent-INRs show downregulation of pro-apoptotic pathways and increased expression of anti-apoptotic molecules that potentially restrain cell turnover¹¹⁶. The blockade of T-cell differentiation from TCM to TEM as a consequence of PD-1 expression could explain the low CD4 T cell numbers observed in these subjects (in contrast to TEM cells which are known to expand and proliferate thereby increasing CD4 cell numbers¹⁰⁶). This limited T-cell turnover in Senescent-INRs could also explain the high frequencies of cells with the multiply spiced HIV RNA, as these cells would accumulate with time. In this manuscript, we provide *ex vivo* and *in vitro* evidence that suggests TGF- β producing Tregs drive impaired T-cell homeostasis and HIV persistence in Senescent-INRs.

The increase in frequencies of TGF- β producing Tregs and activation of signal transduction cascades that lead to upregulation of PML¹¹⁷ and CCNT2 – targets of SMAD2/SMAD3 downstream of TGF- β ^{40,49} establishes cellular quiescence by stabilizing FOXO3 and FOXO4¹¹⁸. This stabilized FOXO4 can bind to p53 to downregulate pro-apoptotic machinery^{45,46}, a major hallmark of senescent cells. *In vitro* validation experiments, in addition to molecular and cellular mechanisms described here implicate TGF- β as the driver of senescence and dysregulated type I IFN-driven pathways (via FOXO3 and IRF3) which impact T-cell homeostasis and promote HIV persistence. In addition, we observe that the senescent INRs have increased expression of the pTEFb complex (comprised of CCNT2 and AFF1) known to support HIV replication^{119,120} and likely aid in further promoting HIV persistence in these subjects.

Finally, in addition to known impact α -ketobutyrate/ β -hydroxybutyrate on FOXO3 upregulation¹²¹, we use *ex vivo* and *in vitro* experiments to demonstrate that naive CD4 T-cells differentiation into GARP + Tregs upon exposure to α -ketobutyrate. These novel findings are in line with previous *in vivo* studies that have shown

increased Treg differentiation upon exposure to butyric acid^{17,104}. The elevated levels of β -hydroxybutyrates (in addition to increase in primary/secondary bile acids) can be produced by the liver during periods of poor dietary intake¹²² and may promote higher inducible HIV (in senescent INRs). Alternately, the increase in plasma butyrates could also be attributed to increased bacterial metabolism¹⁷. In either case, our data suggest that β -hydroxybutyrates drive differentiation of TGF- β producing Tregs - which subsequently leads to CD4 T-cell senescence, lack of CD4 reconstitution and HIV persistence.

Our findings provide a strong rationale for the evaluation of drugs that would target senescent cells^{123,124} as promising therapeutic interventions to reduce the HIV reservoir size. Combination interventions targeting PD-1 and TGF- β , or Senolytics, may have an improved therapeutic impact in Senescent-INRs where frequencies of PD-1 + cells are a correlate of high HIV reservoir and poor CD4 T-cell reconstitution. Interestingly, senescence and TGF- β signaling have been highlighted as hallmarks of cancer where anti-PD-1 therapy has shown efficacy¹²⁵. Our gene classifier could help identify subjects who will not respond to checkpoint therapies in HIV and cancer¹²⁶, and could benefit from interventions that target both PD-1 and TGF- β . Senescent-INRs could also benefit from interventions that promote T-cell differentiation (e.g. IL-15) or rescue the activity of deficient metabolic pathways allowing T-cells to overcome the senescent state and help restore both CD4 T-cell numbers and cell-mediated immunity, which could decrease reservoir size¹²⁷. The multi-omics senescent features and the classifier gene-set described here thus represent critical tools to identify Senescent-INRs. Additionally, the integrated approach used herein holds potential for the identification of novel targets and the design of optimal trials that combine different drugs/biologics targeting senescence and exhaustion to restore immune homeostasis and eradicate HIV.

Experimental Procedures

Study Participants: These studies were approved by the Institutional Review Boards at University Hospitals/Case Medical Center and the Cleveland Clinic Foundation, the Vaccine and Gene Therapy Institute of Florida and University of California San Francisco; all patients provided written informed consent in accordance with the Declaration of Helsinki. **Cohort 1 (CLIF):** A total of 45 immunologic non-responders (INRs) and 17 immune responders (IRs) were identified from the Cleveland Immune Failure cohort. The Cleveland Immune Failure study examined immunologic indices in healthy controls and 2 groups of patients who had been receiving ART for at least 2 years with plasma HIV RNA levels below detectable levels using routine clinical assays; typically, less than 50 copies per milliliter. Transient blips in HIV RNA levels did not exclude participation if flanked by levels below limits of detection. Immune failure patients (INRs) had CD4 T cells <350/ μ L and immune success patients (IRs) had CD4 T cells >500/ μ L. Detailed clinical indices, anti-retroviral regimens and basic demographics are listed in Table S1. **Cohort 2 (SCOPE):** A total of 21 INRs and 20 IRs were identified from the University of California San Francisco (UCSF) SCOPE cohort. Viral suppression was defined by at least two longitudinal tests that showed plasma HIV RNA levels below the limit of detection using standard assays (<40 Abbot RealTime HIV-1 assay, <40 Roche COBAS[®] Ampliprep/COBAS[®] Taqman[®] HIV-1 Test, <50 branched DNA); these tests were done 3 months prior to and on the date of specimen collection. Subjects with viral blips below 200 copies/ml in the time period since beginning ART (or since the end of last treatment gap) 2 years prior to the specimen date were not excluded from the study. Basic demographics and clinical readouts at the time of collection are listed in Table S2.

Microarray Pre-processing and differential gene expression analyses:

Whole blood (from all CLIF and SCOPE participants) was collected and lysed in RLT for RNA extraction (Qiagen, Valencia, CA, USA). CD4+ T (CM, EM, and Innate) cells were FACSsorted from cryopreserved PBMCs directly ex vivo. 7 INRA-A, INR-B and IR subjects (n=42) were collected. These subsets were sorted in 2x buffer for RNA extraction. For the CLIF cohort, cDNA obtained after reverse transcription reaction was hybridized to the Illumina Human HT-12 version 4 Expression BeadChip according to the manufacturer's instruction and quantified using the Illumina iScan System. The data were extracted using the GenomeStudio software. Similarly, the SCOPE cohort samples were run using an Affymetrix microarray system. Detailed analysis of the genome array output data was conducted using the R statistical language¹²⁸ and the Bioconductor suite¹²⁹. Arrays displaying unusually low median expression intensity and variability across all probes relative to all arrays were discarded from the analysis. Probes that do not map to annotated RefSeq genes and control probes were removed. Quantile normalization followed by a log₂ transformation using the Bioconductor package LIMMA was applied to raw microarrays intensities. To determine differences between groups or against a continuous variable, the LIMMA package¹³⁰ was used to fit a linear model to each probe. A (moderated) Student's *t*-test to assess significance in difference between groups, whereas a Pearson correlation test was used to assess significance against a continuous variable. The proportions of false positives were defined using the Benjamini and Hochberg method¹³¹. Unless indicated otherwise, genes that satisfied FDR <0.05 were selected for data mining and functional analyses.

Class identification, classifier training and validation: *Class identification* -In the CLIF cohort, 62 samples were hybridized by the Vaccine Genome Research Institute Genomics Core and 61 samples made it to the downstream analysis (44 INRs and 17 IRs) after outlier identification and removal. Initial exploratory analysis (MDS plot – Fig. 1a) followed by unsupervised analysis (heatmap of top 200 most variable probes – Supplementary Fig. 1c) revealed the discovery of two INR classes in the dataset. The presence of these subject cluster was confirmed when the Gap statistic technique⁸² was used on whole transcriptomic data to determine the optimal number of INR classes. The two classes of INRs were labeled: INR-A (an extreme INR phenotype, n = 15) and INR-B (INR phenotype proximal to IRs, n = 29). Differential expression analyses (described above) were used to identify the differences between IR and INR-A, IR and INR-B and INR-A and INR-B. *Classifier training* -Construction of the INR-A – INR-B Classifier (Fig. 1f, Supplementary Fig. 3) was done using the Prediction Analysis of Microarrays for R (PAM) package from R. PAM uses the nearest shrunken centroid methodology¹³². A standardized centroid for each class (INR-A and INR-B) was computed. Ten-fold cross-validation was used to optimize the shrunken criteria. The shrunken criteria that resulted in the lowest cross-validated misclassification error rate was used to generate the optimized classifier on the CLIF cohort (training cohort). Supplementary Fig. 3a represents training of the 352 features used to build the classifier on the CLIF dataset (see features in Table S11). *Classifier validation* - Testing the classifier on the validation set (SCOPE cohort) is illustrated in Fig. 1f and Fig. 2a. There are no “true” labels that define INR-A or INR-B in the SCOPE testing cohort as they both fall under the label immune non-responders. In order to assess the performance of the classifier on the validation set, the two INR groups had to be defined. An unbiased

unsupervised approach similar to the one used to discover the classes in the CLIF cohort was applied on the normalized Affymetrix microarray data of the SCOPE cohort. Supplementary Fig. 3a shows a heatmap representation of the expression of the top varying probesets (top 200 variant transcripts) on the full SCOPE dataset. Two clusters of INRs were identified using unsupervised clustering (color of branches in Supplementary Fig. 3a denote the discovered classes). This discovery allowed us to label the two subgroups of INRs in the SCOPE cohort. The 352-gene classifier was then applied on the SCOPE cohort. ROC analysis was then used to assess the accuracy (80%) of the classifier on the SCOPE cohort (Fig. 2a). Throughout the study the INR classes in the SCOPE cohort were defined based on the 352-gene classifier (PCA representation of classifier genes in Fig. 2b). Whole transcriptome profiling of classifier defined classes in the SCOPE cohort is shown in Supplementary Fig. 3b.

Pathway analyses. *Gene Set Enrichment Analysis (GSEA)*³⁰ throughout the study was performed to assess enrichment in pathways that discriminated between classes (Fig. 1b-d), were associated with inducible HIV (Supplementary Fig. 5c and Fig. 3e), were associated with Treg cluster 7 (Fig. 3e), were associated with low CD4 counts (Fig. 4e) and were associated with PD1^{hi}ROS^{hi} CD4 TCMs (Fig. 4e, f). Briefly, the whole transcriptome probe-set was collapsed to genes by assessing the most variable probes, pre-ranking of this collapsed transcriptome was done (t-statistic) and enrichment of various genesets was tested after running 1000 permutations of enrichment. *Hallmark MSigDB database*²⁸ (v 7.0) was used to identify pathways that differentiated IR, INR-A and INR-B subjects in the CLIF cohort (Fig. 1b). This database was also used to assess pathways driving lower CD4 counts in the Senescent INRs (Fig. 4e), frequencies of PD^{hi}ROS^{hi} CD4 TCMs in the Senescent INRs (Fig. 4e) and inducible HIV (Table S12) in the SCOPE cohort. *Cell subset deconvolution*: Major peripheral immune subset-specific gene expression signatures were obtained from Nakaya et. al³⁴, and their enrichment was assessed (Fig. 1c, Table S7). In addition, data from a comprehensive study with sorted hematopoietic stem cell-subsets³⁵ was used to generate gene-signatures specific to 38 unique subsets (each subset-specific signature was defined as genes found to be >2-fold higher with p<0.05 than in the pool of all other subsets) (Table S8). These signatures were used to assess variations in differentiated CD4 and CD8 T cell subsets in whole blood in Fig. 1d. *Custom genesets*: Senescence based gene signatures were extracted from Reactome database in MsigDB v7.0's c2 module (Fig. 4f). Genesets specific to host antiviral restriction factors (Supplementary Fig. 6d, Table S12) and IFN signaling (Fig. 1b, Supplementary Fig. 6d, Table S12) were extracted from Abdel-Mohsen et. al¹³³ and Interferome database¹³⁴, respectively. SMAD2/3 and HDAC1/2 genesets were also extracted from MsigDB's c2 module by searching this module for 'SMAD2', 'SMAD3', 'HDAC1' and 'HDAC2'. The results of these analyses are shown in Fig. 3e (Table S17). The enrichment of the 352-geneset classifier gene-set was done where specified (Fig. 1i, Fig. 3e, Table S17). *Leading Edge overlap and Sample Level Enrichment Analyses (SLEA)*: Leading edge genes from the analyses above were overlapped (significance of overlap was determined using Fischer's Exact test; p < 0.05) to define new gene-lists that were associated with both "inducible HIV and Treg cluster 17" (Fig. 3e, Table S17) OR "CD4 counts and PD1^{hi}ROS^{hi} CD4 TCMs" (Fig. 4e, Table S20). SLEA was used to generate a z-score normalized value for genelists in Fig. 3e, 4e and 4f. These scores were correlated (spearman correlation test) with each other, minor (Treg frequencies and PD1^{hi}ROS^{hi} CD4 TCM frequencies) and major (inducible HIV and CD4 counts) outcomes to generate the integrated correlation network model in Fig. 6e and Table S20.

Over-representation, gene-mania/correlation networks and transcription Factor (TF) analyses: *Over-representation* of Reactome pathways in genes that are upregulated in the INR-As (vs both IRs and INR-Bs; FDR < 0.05) was assessed using the ClueGO plug-in from Cytoscape (<http://apps.cytoscape.org/apps/cluego>³⁶), and the results of these analyses were corrected for multiple comparisons using Bonferroni step-down correction (Fig. 1e, see Table S10 for full results). *GeneMania and correlations network:* GeneMania Networks¹³⁵ (<http://genemania.org>) were plotted to represent co-expression of genes (Supplementary Fig. 2b and Supplementary Fig. 2d). Overlap between the genes included in the networks and Gene Ontology (GO) biological process was assessed using a Fisher exact test. Correlation networks in Fig. 3d, Fig. 4d, Fig. 6e and Supplementary Fig. 5c are based on significant Spearman correlations (p-value < 0.05) between the features indicated in each figure. All networks were plotted using the Cytoscape Plug-in – specific value/category for all nodes and edges are available upon request. *Transcription factor list* was generated by combining genes with known ChIP-seq validated targets from CHEA¹³⁶ (<https://amp.pharm.mssm.edu/Harmonizome/resource/ChIP-X+Enrichment+Analysis>) and ENCODE (<https://amp.pharm.mssm.edu/Harmonizome/dataset/ENCODE+Transcription+Factor+Targets>) databases. The expression of these TFs was tested in INR-As vs INR-Bs or IRs (Supplementary Fig. 2c). IRF3 targets and FOXO3 targets were extracted from the ENCODE and CHEA databases cited above, respectively. Co-expressed targets of FOXO3 and IRF3 that correlated with inducible HIV are represented in Fig. 6d (Table S12).

Cell Preparation and flow cytometry: PBMCs were prepared from whole blood by ficoll-hypaque density sedimentation and cryopreserved in 10% dimethyl sulfoxide and 90% FBS. Two panels to evaluate Treg function and mitochondrial dysfunction in memory CD4s were run using previously titrated antibodies summarized in Table S13, S14 and S18. The cells were surface stained for 20 minutes in the dark at room temperature, washed, fixed and permeabilized using the eBioscience™ Foxp3 / Transcription Factor Staining Buffer Set (Cat# 00-5523-00), as per manufacture instructions. Intracellular staining was performed in Perm-Wash provided by the kit for 45 minutes at 4°C. Samples were washed and re-suspended in staining buffer for acquisition. ~500,000 live-gated events were collected per sample on the LSRII flow cytometer (Becton Dickinson, San Jose, CA). Initial data cleaning and pre-gating was done using the Flow-Jo X software (TreeStar, Ashland, OR) (Supplementary Fig. 7). Briefly, lymphocyte gate based on FSC-A and SSC-A was defined. Single cells were then selected using a FSC-A x FCS-H gate. Live CD3+CD4+CD8- cells were gated and exported for unbiased clustering analyses (Supplementary Fig. 7). For both panels, projection of the density of cells expressing markers of interest (Table S14, Table S18) were visualized/plotted on a 2-dimensional UMAP (<https://arxiv.org/abs/1802.03426>, <https://github.com/lmcinnes/umap>). Clusters of cells using the RPhenograph package after (<https://github.com/jacoblevine/PhenoGraph>) after concatenating all samples per panel and bi-exponentially transforming each marker (Fig. 3a and c, Fig. 4a). Differences in cluster frequencies per group and MFI for each marker per cluster, for each are shown in Table S14 and Table S18.

Measurement of inducible reservoir: The HIV reservoir was measured using the tat/rev induced limiting dilution assay (TILDA). This method measures the inducible reservoir by RT-qPCR using the limiting dilution assay previously described⁷³. Briefly, 2×10^6 CD4 T cells from 20×10^6 PBMCs were enriched using a CD4 T cell negative selection kit (Stem Cell). These cells were stimulated with PMA/Iono (100ng/ml and 1 μ g/ml, respectively) for 12 hours. A total of 744,000 stimulated cells were then distributed in a limiting dilution in a 96-well plate and tat/rev msRNA expression was directly quantified (without prior RNA extraction) by semi-nested real-time PCR⁷³. The frequencies of cells positive for inducible tat/rev msRNA per 10^6 CD4+ T cells were determined by using the maximum likelihood method (<http://bioinf.wehi.edu.au/software/elda>) (Fig. 2 c,d).

Measurement of plasma biomarkers: Plasma IL-6 in the CLIF cohort was measured using a high sensitivity ELISA kit for human IL-6 (Quantikine HS) from R&D Systems (Minneapolis, MN). Plasma levels of IL-7 in the CLIF cohort were measured by high sensitivity IL-7 ELISA (Quantikine HS, R&D Systems, Minneapolis, MN). Plasma levels of IP10 in the CLIF cohort were measured by IP-10 ELISA (Quantikine, R&D Systems, Minneapolis, MN). Plasma levels of human Intestinal Fatty Acid Binding Protein (I-FABP) in the CLIF cohort were measured using a DuoSet ELISA Development kit from R&D Systems (Minneapolis, MN) following the manufacturer's protocol. Levels of D-dimers in the CLIF cohort were measured using the Asserachrom D-DI immunoassay (Diagnostica Stago, Asnieres France) (Supplementary Fig 1. d-m). Measurement of LPS in the CLIF cohort: Plasma samples were diluted to 10% or 20% with endotoxin free water and then heated to 85°C for 15 minutes to denature plasma proteins. We then quantified plasma levels of LPS with a commercially available Limulus Amebocyte Lysate (LAL) assay (QCL-1000, Lonza, Walkersville, MD) according to the manufacturer's protocol. Multiplex ELISA (Mesoscale): U-PLEX assay (Meso Scale MULTI-ARRAY Technology) commercially available by Meso Scale Discovery (MSD) was used for plasma cytokine detection. The assay was performed according to the manufacturer's instructions (https://www.mesoscale.com/en/technical_resources/technical_literature/technical_notes_search). 25 μ L of plasma from each donor was combined with the biotinylated antibody plus the assigned linker and the SULFO-TAG™ conjugated detection antibody; in parallel a multi-analyte calibrator standard was prepared by doing 4-fold serial dilutions. Both samples and calibrators were mixed with the Read buffer and loaded in a 10-spot U-PLEX plate, which was read by the MESO QuickPlex SQ 120. The plasma cytokines values (pg/mL) were extrapolated from the standard curve of each specific analyte. Cytokine clustering (Supplementary Fig. 4a,b,c) was performed using independent methods: (gap statistic method to identify and characterize optimal number of k-means clusters, and hierarchical clustering (ward clustering; Euclidean distance⁸²).

Metabolome. In collaboration with Metabolon, plasma metabolite levels for up to 1300 metabolites were measured. Metabolon uses four ultra-high-performance liquid chromatography/tandem accurate mass spectrometry (UHPLC/MS/MS) methods in a highly controlled environment to reduce noise and produce accurate results. The data generated using UHPLC/MS/MS were referenced against a well-established library of known and novel metabolites.

Treg differentiation in the presence of alpha-ketobutyrate: Naïve CD4 T cells extracted from 8 healthy donors were isolated using the EasySep™ Human Naïve CD4+ T Cell Isolation Kit (StemCell Technologies Catalog# 19555) and differentiated in vitro using the protocols described by Rudensky¹⁰⁴. Briefly, 100-200,000 naïve CD4 T cells were stimulated with Dynabeads Human T-Activator CD3/CD28 beads (ThermoFisher Scientific Cat# 111.31D, 1 bead/3 cells), 100 U/mL of IL-2 (R&D Systems Cat# 202-IL-500), 0 to 1ng/mL of TGF-b (R&D Systems Cat# 240-B-010) and alpha-ketobutyrate (Cat#, from 0mM to 5mM) for 3 days in 96-well round bottom plates. Viability post-stimulation, assessed post-stimulation by staining with a fixable viability dye, was found to be >80% in all stimulation conditions. Secreted cytokines in the supernatants were quantified using the Mesoscale Discovery platform/kits described above. CD4 T cells were intracellularly stained with the Treg phenotyping panel described (Table. S8).

Latency establishment and reactivation assay: The latency and reactivation assays developed by our group¹⁰⁶ was used to assess the latency establishment in memory CD4 T cells post-stimulation with increasing doses of TGF-b. Briefly, memory CD4 T cells spinoculated with HIV (HIV strain information listed¹⁰⁶) were incubated in the presence of antiretrovirals (effavirenz, Saquinavir and Raltegravir) and latency establishment media (supplemented with 0-40ng/mL of TGF-b) for 13 days (or when the frequencies of HIV-p24+, measured by flow cytometry, CD4 T cells was negligible). Integrated HIV DNA was measured at this stage using the protocol described¹⁰⁶. Reactivation of HIV post-latency was done after stimulation with 1ug/mL anti-CD3 and 1ug/mL of anti-CD28 for ~48 hours; reactivated cells were quantified by monitoring the frequencies of p24+ cells using flow cytometry.

Other statistical analyses: All univariate group-differences were analyzed using a non-parametric Wilcoxon-ranked test. All univariate correlation analyses were done using a non-parametric Spearman's test. P<0.05 is reported as significant.

Declarations

Full Data Availability Statement: The raw and normalized data matrices for gene expression analysis of the CLIF and SCOPE cohorts were deposited into the Gene Expression Omnibus (GEO) database; GSE143742.

Financial support: This work was supported by the National Institutes of Health (grants U01 AI 105937 and RO1 AI 110334 and RO1 AI 11444201), the CWRU Center for AIDS Research (grant AI 36219), DARE (U19 AI 096109), and the Fasnemyer Foundation. Rafick-Pierre Sekaly is the Richard J. Fasnemyer Professor of Immunopathogenesis.

Potential conflicts of interest: All authors: No reported conflicts

References

1. Dimitrov, D. T., Kiem, H. P., Jerome, K. R., Johnston, C. & Schiffer, J. T. A curative regimen would decrease HIV prevalence but not HIV incidence unless targeted to an ART-naive population. *Sci Rep* **6**, 22183, doi:10.1038/srep22183 (2016).
2. Chu, C., Umanski, G., Blank, A., Grossberg, R. & Selwyn, P. A. HIV-infected patients and treatment outcomes: an equivalence study of community-located, primary care-based HIV treatment vs. hospital-based specialty care in the Bronx, New York. *AIDS Care* **22**, 1522–1529, doi:10.1080/09540121.2010.484456 (2010).
3. Yang, X. *et al.* Incomplete immune reconstitution in HIV/AIDS patients on antiretroviral therapy: Challenges of immunological non-responders. *J Leukoc Biol* **107**, 597–612, doi:10.1002/JLB.4MR1019-189R (2020).
4. Gaardbo, J. C., Hartling, H. J., Gerstoft, J. & Nielsen, S. D. Incomplete immune recovery in HIV infection: mechanisms, relevance for clinical care, and possible solutions. *Clin Dev Immunol* **2012**, 670957, doi:10.1155/2012/670957 (2012).
5. Massanella, M., Negredo, E., Clotet, B. & Blanco, J. Immunodiscordant responses to HAART—mechanisms and consequences. *Expert Rev Clin Immunol* **9**, 1135–1149, doi:10.1586/1744666X.2013.842897 (2013).
6. Pacheco, Y. M. *et al.* Increased risk of non-AIDS-related events in HIV subjects with persistent low CD4 counts despite cART in the CoRIS cohort. *Antiviral Res* **117**, 69–74, doi:10.1016/j.antiviral.2015.03.002 (2015).
7. Mendez-Lagares, G. *et al.* Specific patterns of CD4-associated immunosenescence in vertically HIV-infected subjects. *Clin Microbiol Infect* **19**, 558–565, doi:10.1111/j.1469-0691.2012.03934.x (2013).
8. Grabmeier-Pfistershammer, K., Steinberger, P., Rieger, A., Leitner, J. & Kohrgruber, N. Identification of PD-1 as a unique marker for failing immune reconstitution in HIV-1-infected patients on treatment. *J Acquir Immune Defic Syndr* **56**, 118–124, doi:10.1097/QAI.0b013e3181fbab9f (2011).
9. Mendez-Lagares, G. *et al.* Severe immune dysregulation affects CD4(+)CD25(hi)FoxP3(+) regulatory T cells in HIV-infected patients with low-level CD4 T-cell repopulation despite suppressive highly active antiretroviral therapy. *J Infect Dis* **205**, 1501–1509, doi:10.1093/infdis/jis230 (2012).
10. Lederman, M. M., Funderburg, N. T., Sekaly, R. P., Klatt, N. R. & Hunt, P. W. Residual immune dysregulation syndrome in treated HIV infection. *Adv Immunol* **119**, 51–83, doi:10.1016/B978-0-12-407707-2.00002-3 (2013).
11. Boulassel, M. R. *et al.* CD4 T cell nadir independently predicts the magnitude of the HIV reservoir after prolonged suppressive antiretroviral therapy. *J Clin Virol* **53**, 29–32, doi:10.1016/j.jcv.2011.09.018 (2012).
12. Said, E. A. *et al.* Programmed death-1-induced interleukin-10 production by monocytes impairs CD4 + T cell activation during HIV infection. *Nat Med* **16**, 452–459, doi:10.1038/nm.2106 (2010).
13. Shive, C. L. *et al.* Inflammation Perturbs the IL-7 Axis, Promoting Senescence and Exhaustion that Broadly Characterize Immune Failure in Treated HIV Infection. *J Acquir Immune Defic Syndr* **71**, 483–492, doi:10.1097/QAI.0000000000000913 (2016).
14. Molina-Pinelo, S. *et al.* Premature immunosenescence in HIV-infected patients on highly active antiretroviral therapy with low-level CD4 T cell repopulation. *J Antimicrob Chemother* **64**, 579–588, doi:10.1093/jac/dkp248 (2009).

15. Guo, H. *et al.* Multi-omics analyses reveal that HIV-1 alters CD4(+) T cell immunometabolism to fuel virus replication. *Nat Immunol* **22**, 423–433, doi:10.1038/s41590-021-00898-1 (2021).
16. Hang, S. *et al.* Bile acid metabolites control TH17 and Treg cell differentiation. *Nature* **576**, 143–148, doi:10.1038/s41586-019-1785-z (2019).
17. Furusawa, Y. *et al.* Commensal microbe-derived butyrate induces the differentiation of colonic regulatory T cells. *Nature* **504**, 446–450, doi:10.1038/nature12721 (2013).
18. Hiener, B. *et al.* Identification of Genetically Intact HIV-1 Proviruses in Specific CD4(+) T Cells from Effectively Treated Participants. *Cell Rep* **21**, 813–822, doi:10.1016/j.celrep.2017.09.081 (2017).
19. Churchill, M. J., Deeks, S. G., Margolis, D. M., Siliciano, R. F. & Swanstrom, R. HIV reservoirs: what, where and how to target them. *Nat Rev Microbiol* **14**, 55–60, doi:10.1038/nrmicro.2015.5 (2016).
20. Peluso, M. J. *et al.* Differential decay of intact and defective proviral DNA in HIV-1-infected individuals on suppressive antiretroviral therapy. *JCI Insight* **5**, doi:10.1172/jci.insight.132997 (2020).
21. Freeman, M. L. *et al.* Cytokines and T-Cell Homeostasis in HIV Infection. *J Infect Dis* **214 Suppl 2**, S51–57, doi:10.1093/infdis/jiw287 (2016).
22. von Stockenstrom, S. *et al.* Longitudinal Genetic Characterization Reveals That Cell Proliferation Maintains a Persistent HIV Type 1 DNA Pool During Effective HIV Therapy. *J Infect Dis* **212**, 596–607, doi:10.1093/infdis/jiv092 (2015).
23. Chomont, N., DaFonseca, S., Vandergeeten, C., Ancuta, P. & Sekaly, R. P. Maintenance of CD4 + T-cell memory and HIV persistence: keeping memory, keeping HIV. *Curr Opin HIV AIDS* **6**, 30–36, doi:10.1097/COH.0b013e3283413775 (2011).
24. Chomont, N. *et al.* HIV reservoir size and persistence are driven by T cell survival and homeostatic proliferation. *Nat Med* **15**, 893–900, doi:10.1038/nm.1972 (2009).
25. Fromentin, R. *et al.* PD-1 blockade potentiates HIV latency reversal ex vivo in CD4(+) T cells from ART-suppressed individuals. *Nat Commun* **10**, 814, doi:10.1038/s41467-019-08798-7 (2019).
26. Fromentin, R. *et al.* CD4 + T Cells Expressing PD-1, TIGIT and LAG-3 Contribute to HIV Persistence during ART. *PLoS Pathog* **12**, e1005761, doi:10.1371/journal.ppat.1005761 (2016).
27. Borges, A. H. *et al.* Factors Associated With Plasma IL-6 Levels During HIV Infection. *J Infect Dis* **212**, 585–595, doi:10.1093/infdis/jiv123 (2015).
28. Liberzon, A. *et al.* The Molecular Signatures Database (MSigDB) hallmark gene set collection. *Cell Syst* **1**, 417–425, doi:10.1016/j.cels.2015.12.004 (2015).
29. Liberzon, A. *et al.* Molecular signatures database (MSigDB) 3.0. *Bioinformatics* **27**, 1739–1740, doi:10.1093/bioinformatics/btr260 (2011).
30. Subramanian, A. *et al.* Gene set enrichment analysis: a knowledge-based approach for interpreting genome-wide expression profiles. *Proc Natl Acad Sci U S A* **102**, 15545–15550, doi:10.1073/pnas.0506580102 (2005).
31. Prieto, L. I., Graves, S. I. & Baker, D. J. Insights from In Vivo Studies of Cellular Senescence. *Cells* **9**, doi:10.3390/cells9040954 (2020).
32. Childs, B. G., Durik, M., Baker, D. J. & van Deursen, J. M. Cellular senescence in aging and age-related disease: from mechanisms to therapy. *Nat Med* **21**, 1424–1435, doi:10.1038/nm.4000 (2015).

33. Wang, R. *et al.* The transcription factor Myc controls metabolic reprogramming upon T lymphocyte activation. *Immunity* **35**, 871–882, doi:10.1016/j.immuni.2011.09.021 (2011).
34. Nakaya, H. I. *et al.* Systems biology of vaccination for seasonal influenza in humans. *Nat Immunol* **12**, 786–795, doi:10.1038/ni.2067 (2011).
35. Novershtern, N. *et al.* Densely interconnected transcriptional circuits control cell states in human hematopoiesis. *Cell* **144**, 296–309, doi:10.1016/j.cell.2011.01.004 (2011).
36. Bindea, G. *et al.* ClueGO: a Cytoscape plug-in to decipher functionally grouped gene ontology and pathway annotation networks. *Bioinformatics* **25**, 1091–1093, doi:10.1093/bioinformatics/btp101 (2009).
37. Jassal, B. *et al.* The reactome pathway knowledgebase. *Nucleic Acids Res* **48**, D498–D503, doi:10.1093/nar/gkz1031 (2020).
38. Douagi, I. *et al.* Role of interferon regulatory factor 3 in type I interferon responses in rotavirus-infected dendritic cells and fibroblasts. *J Virol* **81**, 2758–2768, doi:10.1128/JVI.01555-06 (2007).
39. Webb, A. E. & Brunet, A. FOXO transcription factors: key regulators of cellular quality control. *Trends Biochem Sci* **39**, 159–169, doi:10.1016/j.tibs.2014.02.003 (2014).
40. Nakao, A. *et al.* TGF-beta receptor-mediated signalling through Smad2, Smad3 and Smad4. *EMBO J* **16**, 5353–5362, doi:10.1093/emboj/16.17.5353 (1997).
41. Ramakrishnan, R. *et al.* Identification of novel CDK9 and Cyclin T1-associated protein complexes (CCAPs) whose siRNA depletion enhances HIV-1 Tat function. *Retrovirology* **9**, 90, doi:10.1186/1742-4690-9-90 (2012).
42. Chang, Z. S. *et al.* Forkhead box O3 protects the heart against paraquat-induced aging-associated phenotypes by upregulating the expression of antioxidant enzymes. *Aging Cell* **18**, e12990, doi:10.1111/accel.12990 (2019).
43. Nho, R. S. & Hergert, P. FoxO3a and disease progression. *World J Biol Chem* **5**, 346–354, doi:10.4331/wjbc.v5.i3.346 (2014).
44. Hagenbuchner, J. & Ausserlechner, M. J. Mitochondria and FOXO3: breath or die. *Front Physiol* **4**, 147, doi:10.3389/fphys.2013.00147 (2013).
45. Bourgeois, B. & Madl, T. Regulation of cellular senescence via the FOXO4-p53 axis. *FEBS Lett* **592**, 2083–2097, doi:10.1002/1873-3468.13057 (2018).
46. Baar, M. P. *et al.* Targeted Apoptosis of Senescent Cells Restores Tissue Homeostasis in Response to Chemotoxicity and Aging. *Cell* **169**, 132–147 e116, doi:10.1016/j.cell.2017.02.031 (2017).
47. Hagenbuchner, J. *et al.* FOXO3-induced reactive oxygen species are regulated by BCL2L11 (Bim) and SESN3. *J Cell Sci* **125**, 1191–1203, doi:10.1242/jcs.092098 (2012).
48. Fu, Z. & Tindall, D. J. FOXOs, cancer and regulation of apoptosis. *Oncogene* **27**, 2312–2319, doi:10.1038/onc.2008.24 (2008).
49. Lin, H. K., Bergmann, S. & Pandolfi, P. P. Cytoplasmic PML function in TGF-beta signalling. *Nature* **431**, 205–211, doi:10.1038/nature02783 (2004).
50. Lusic, M. *et al.* Proximity to PML nuclear bodies regulates HIV-1 latency in CD4 + T cells. *Cell Host Microbe* **13**, 665–677, doi:10.1016/j.chom.2013.05.006 (2013).

51. Brown, J. A. *et al.* TGF-beta-Induced Quiescence Mediates Chemoresistance of Tumor-Propagating Cells in Squamous Cell Carcinoma. *Cell Stem Cell* **21**, 650–664 e658, doi:10.1016/j.stem.2017.10.001 (2017).
52. Yang, L. *et al.* Targeting Stromal Glutamine Synthetase in Tumors Disrupts Tumor Microenvironment-Regulated Cancer Cell Growth. *Cell Metab* **24**, 685–700, doi:10.1016/j.cmet.2016.10.011 (2016).
53. van der Vos, K. E. & Coffey, P. J. Glutamine metabolism links growth factor signaling to the regulation of autophagy. *Autophagy* **8**, 1862–1864, doi:10.4161/auto.22152 (2012).
54. Dang, C. V. c-Myc target genes involved in cell growth, apoptosis, and metabolism. *Mol Cell Biol* **19**, 1–11, doi:10.1128/mcb.19.1.1 (1999).
55. Richmond, A. Nf-kappa B, chemokine gene transcription and tumour growth. *Nat Rev Immunol* **2**, 664–674, doi:10.1038/nri887 (2002).
56. He, Y., Hara, H. & Nunez, G. Mechanism and Regulation of NLRP3 Inflammasome Activation. *Trends Biochem Sci* **41**, 1012–1021, doi:10.1016/j.tibs.2016.09.002 (2016).
57. Barkett, M. & Gilmore, T. D. Control of apoptosis by Rel/NF-kappaB transcription factors. *Oncogene* **18**, 6910–6924, doi:10.1038/sj.onc.1203238 (1999).
58. Herranz, N. & Gil, J. Mechanisms and functions of cellular senescence. *J Clin Invest* **128**, 1238–1246, doi:10.1172/JCI95148 (2018).
59. Baar, M. P., Van Willigenburg, H. & de Keizer, P. L. J. Maintenance and repair of an aging life cycle. *Oncotarget* **8**, 86985–86986, doi:10.18632/oncotarget.18046 (2017).
60. Borrás, C. *et al.* BCL-xL, a Mitochondrial Protein Involved in Successful Aging: From C. elegans to Human Centenarians. *Int J Mol Sci* **21**, doi:10.3390/ijms21020418 (2020).
61. Feng, J. *et al.* R1OK3 is an adaptor protein required for IRF3-mediated antiviral type I interferon production. *J Virol* **88**, 7987–7997, doi:10.1128/JVI.00643-14 (2014).
62. Suhane, S., Kanzaki, H., Arumugaswami, V., Murali, R. & Ramanujan, V. K. Mitochondrial NDUFS3 regulates the ROS-mediated onset of metabolic switch in transformed cells. *Biol Open* **2**, 295–305, doi:10.1242/bio.20133244 (2013).
63. Ji, L. *et al.* Slc6a8-Mediated Creatine Uptake and Accumulation Reprogram Macrophage Polarization via Regulating Cytokine Responses. *Immunity* **51**, 272–284 e277, doi:10.1016/j.immuni.2019.06.007 (2019).
64. Khan, A. A. & Quigley, J. G. Heme and FLVCR-related transporter families SLC48 and SLC49. *Mol Aspects Med* **34**, 669–682, doi:10.1016/j.mam.2012.07.013 (2013).
65. Reithmeier, R. A. *et al.* Band 3, the human red cell chloride/bicarbonate anion exchanger (AE1, SLC4A1), in a structural context. *Biochim Biophys Acta* **1858**, 1507–1532, doi:10.1016/j.bbamem.2016.03.030 (2016).
66. Hoffman, N. E. *et al.* SLC25A23 augments mitochondrial Ca(2)(+) uptake, interacts with MCU, and induces oxidative stress-mediated cell death. *Mol Biol Cell* **25**, 936–947, doi:10.1091/mbc.E13-08-0502 (2014).
67. Kim, J. *et al.* Amino Acid Transporter Slc38a5 Controls Glucagon Receptor Inhibition-Induced Pancreatic alpha Cell Hyperplasia in Mice. *Cell Metab* **25**, 1348–1361 e1348, doi:10.1016/j.cmet.2017.05.006 (2017).
68. Hoffmann, E. K. & Dunham, P. B. Membrane mechanisms and intracellular signalling in cell volume regulation. *Int Rev Cytol* **161**, 173–262, doi:10.1016/s0074-7696(08)62498-5 (1995).
69. Hamill, O. P. & Martinac, B. Molecular basis of mechanotransduction in living cells. *Physiol Rev* **81**, 685–740, doi:10.1152/physrev.2001.81.2.685 (2001).

70. Neurohr, G. E. *et al.* Excessive Cell Growth Causes Cytoplasm Dilution And Contributes to Senescence. *Cell* **176**, 1083–1097 e1018, doi:10.1016/j.cell.2019.01.018 (2019).
71. Yamakami, Y. *et al.* High concentrations of NaCl induce cell swelling leading to senescence in human cells. *Mol Cell Biochem* **411**, 117–125, doi:10.1007/s11010-015-2573-1 (2016).
72. Klatt, N. R., Chomont, N., Douek, D. C. & Deeks, S. G. Immune activation and HIV persistence: implications for curative approaches to HIV infection. *Immunol Rev* **254**, 326–342, doi:10.1111/imr.12065 (2013).
73. Procopio, F. A. *et al.* A Novel Assay to Measure the Magnitude of the Inducible Viral Reservoir in HIV-infected Individuals. *EBioMedicine* **2**, 874–883, doi:10.1016/j.ebiom.2015.06.019 (2015).
74. Haxhinasto, S., Mathis, D. & Benoist, C. The AKT-mTOR axis regulates de novo differentiation of CD4 + Foxp3 + cells. *J Exp Med* **205**, 565–574, doi:10.1084/jem.20071477 (2008).
75. Wan, Y. Y. & Flavell, R. A. TGF-beta and regulatory T cell in immunity and autoimmunity. *J Clin Immunol* **28**, 647–659, doi:10.1007/s10875-008-9251-y (2008).
76. Kitagawa, Y. *et al.* Guidance of regulatory T cell development by Satb1-dependent super-enhancer establishment. *Nat Immunol* **18**, 173–183, doi:10.1038/ni.3646 (2017).
77. Salvany-Celades, M. *et al.* Three Types of Functional Regulatory T Cells Control T Cell Responses at the Human Maternal-Fetal Interface. *Cell Rep* **27**, 2537–2547 e2535, doi:10.1016/j.celrep.2019.04.109 (2019).
78. Dedobbeleer, O., Stockis, J., van der Woning, B., Coulie, P. G. & Lucas, S. Cutting Edge: Active TGF-beta1 Released from GARP/TGF-beta1 Complexes on the Surface of Stimulated Human B Lymphocytes Increases Class-Switch Recombination and Production of IgA. *J Immunol* **199**, 391–396, doi:10.4049/jimmunol.1601882 (2017).
79. Tran, D. Q. *et al.* GARP (LRRC32) is essential for the surface expression of latent TGF-beta on platelets and activated FOXP3 + regulatory T cells. *Proc Natl Acad Sci U S A* **106**, 13445–13450, doi:10.1073/pnas.0901944106 (2009).
80. Levine, J. H. *et al.* Data-Driven Phenotypic Dissection of AML Reveals Progenitor-like Cells that Correlate with Prognosis. *Cell* **162**, 184–197, doi:10.1016/j.cell.2015.05.047 (2015).
81. Huang, W., Solouki, S., Carter, C., Zheng, S. G. & August, A. Beyond Type 1 Regulatory T Cells: Co-expression of LAG3 and CD49b in IL-10-Producing T Cell Lineages. *Front Immunol* **9**, 2625, doi:10.3389/fimmu.2018.02625 (2018).
82. Tibshirani, R., Walther, G. & Hastie, T. Estimating the number of clusters in a data set via the gap statistic. *J R Stat Soc B* **63**, 411–423, doi:Doi 10.1111/1467-9868.00293 (2001).
83. Oh, S. A. & Li, M. O. TGF-beta: guardian of T cell function. *J Immunol* **191**, 3973–3979, doi:10.4049/jimmunol.1301843 (2013).
84. Wynn, T. A. IL-13 effector functions. *Annu Rev Immunol* **21**, 425–456, doi:10.1146/annurev.immunol.21.120601.141142 (2003).
85. Boro, M. & Balaji, K. N. CXCL1 and CXCL2 Regulate NLRP3 Inflammasome Activation via G-Protein-Coupled Receptor CXCR2. *J Immunol* **199**, 1660–1671, doi:10.4049/jimmunol.1700129 (2017).
86. Gupta, K. *et al.* VEGF prevents apoptosis of human microvascular endothelial cells via opposing effects on MAPK/ERK and SAPK/JNK signaling. *Exp Cell Res* **247**, 495–504, doi:10.1006/excr.1998.4359 (1999).

87. Cohen, S. B. IL-10 and IL-3 synergize to cause proliferation of human T cells. *Immunology* **85**, 351–356 (1995).
88. Li, W. Q. *et al.* IL-7 promotes T cell proliferation through destabilization of p27Kip1. *J Exp Med* **203**, 573–582, doi:10.1084/jem.20051520 (2006).
89. Koinuma, D. *et al.* Chromatin immunoprecipitation on microarray analysis of Smad2/3 binding sites reveals roles of ETS1 and TFAP2A in transforming growth factor beta signaling. *Mol Cell Biol* **29**, 172–186, doi:10.1128/MCB.01038-08 (2009).
90. Senese, S. *et al.* Role for histone deacetylase 1 in human tumor cell proliferation. *Mol Cell Biol* **27**, 4784–4795, doi:10.1128/MCB.00494-07 (2007).
91. Dubois, C. M. *et al.* Evidence that furin is an authentic transforming growth factor-beta1-converting enzyme. *Am J Pathol* **158**, 305–316, doi:10.1016/s0002-9440(10)63970-3 (2001).
92. Vallee, A., Lecarpentier, Y., Guillevin, R. & Vallee, J. N. Interactions between TGF-beta1, canonical WNT/beta-catenin pathway and PPAR gamma in radiation-induced fibrosis. *Oncotarget* **8**, 90579–90604, doi:10.18632/oncotarget.21234 (2017).
93. Xu, L. *et al.* Activation of Wnt/beta-catenin signalling is required for TGF-beta/Smad2/3 signalling during myofibroblast proliferation. *J Cell Mol Med* **21**, 1545–1554, doi:10.1111/jcmm.13085 (2017).
94. Kleinsimon, S. *et al.* GADD45A and CDKN1A are involved in apoptosis and cell cycle modulatory effects of viscumTT with further inactivation of the STAT3 pathway. *Sci Rep* **8**, 5750, doi:10.1038/s41598-018-24075-x (2018).
95. Park, B. V. *et al.* TGFbeta1-Mediated SMAD3 Enhances PD-1 Expression on Antigen-Specific T Cells in Cancer. *Cancer Discov* **6**, 1366–1381, doi:10.1158/2159-8290.CD-15-1347 (2016).
96. Ferber, E. C. *et al.* FOXO3a regulates reactive oxygen metabolism by inhibiting mitochondrial gene expression. *Cell Death Differ* **19**, 968–979, doi:10.1038/cdd.2011.179 (2012).
97. Shytaj, I. L. *et al.* Alterations of redox and iron metabolism accompany the development of HIV latency. *EMBO J* **39**, e102209, doi:10.15252/embj.2019102209 (2020).
98. Hatano, H. *et al.* Cell-based measures of viral persistence are associated with immune activation and programmed cell death protein 1 (PD-1)-expressing CD4 + T cells. *J Infect Dis* **208**, 50–56, doi:10.1093/infdis/jis630 (2013).
99. Corral-Jara, K. F., Rosas da Silva, G., Fierro, N. A. & Soumelis, V. Modeling the Th17 and Tregs Paradigm: Implications for Cancer Immunotherapy. *Front Cell Dev Biol* **9**, 675099, doi:10.3389/fcell.2021.675099 (2021).
100. Bettini, M. & Bettini, M. L. Function, Failure, and the Future Potential of Tregs in Type 1 Diabetes. *Diabetes* **70**, 1211–1219, doi:10.2337/dbi18-0058 (2021).
101. Beppu, L. Y. *et al.* Tregs facilitate obesity and insulin resistance via a Blimp-1/IL-10 axis. *JCI Insight* **6**, doi:10.1172/jci.insight.140644 (2021).
102. Ali, A. J., Makings, J. & Ley, K. Regulatory T Cell Stability and Plasticity in Atherosclerosis. *Cells* **9**, doi:10.3390/cells9122665 (2020).
103. Zeng, Q. *et al.* A Unique Population: Adipose-Resident Regulatory T Cells. *Front Immunol* **9**, 2075, doi:10.3389/fimmu.2018.02075 (2018).

104. Arpaia, N. *et al.* Metabolites produced by commensal bacteria promote peripheral regulatory T-cell generation. *Nature* **504**, 451–455, doi:10.1038/nature12726 (2013).
105. Li, C., Ebert, P. J. & Li, Q. J. T cell receptor (TCR) and transforming growth factor beta (TGF-beta) signaling converge on DNA (cytosine-5)-methyltransferase to control forkhead box protein 3 (foxp3) locus methylation and inducible regulatory T cell differentiation. *J Biol Chem* **288**, 19127–19139, doi:10.1074/jbc.M113.453357 (2013).
106. Kulpa, D. A. *et al.* Differentiation into an Effector Memory Phenotype Potentiates HIV-1 Latency Reversal in CD4(+) T Cells. *J Virol* **93**, doi:10.1128/JVI.00969-19 (2019).
107. Janumyan, Y. M. *et al.* Bcl-xL/Bcl-2 coordinately regulates apoptosis, cell cycle arrest and cell cycle entry. *EMBO J* **22**, 5459–5470, doi:10.1093/emboj/cdg533 (2003).
108. Klotz, L. O. *et al.* Redox regulation of FoxO transcription factors. *Redox Biol* **6**, 51–72, doi:10.1016/j.redox.2015.06.019 (2015).
109. Marinkovic, D. *et al.* Foxo3 is required for the regulation of oxidative stress in erythropoiesis. *J Clin Invest* **117**, 2133–2144, doi:10.1172/JCI31807 (2007).
110. Dong, H. *et al.* Role of FOXO3 Activated by HIV-1 Tat in HIV-Associated Neurocognitive Disorder Neuronal Apoptosis. *Front Neurosci* **13**, 44, doi:10.3389/fnins.2019.00044 (2019).
111. Jin, S. M. & Youle, R. J. PINK1- and Parkin-mediated mitophagy at a glance. *J Cell Sci* **125**, 795–799, doi:10.1242/jcs.093849 (2012).
112. Sasai, M. *et al.* Essential role for GABARAP autophagy proteins in interferon-inducible GTPase-mediated host defense. *Nat Immunol* **18**, 899–910, doi:10.1038/ni.3767 (2017).
113. Hopkins, B. L. & Neumann, C. A. Redoxins as gatekeepers of the transcriptional oxidative stress response. *Redox Biol* **21**, 101104, doi:10.1016/j.redox.2019.101104 (2019).
114. Trautmann, L. *et al.* Upregulation of PD-1 expression on HIV-specific CD8 + T cells leads to reversible immune dysfunction. *Nat Med* **12**, 1198–1202, doi:10.1038/nm1482 (2006).
115. Odorizzi, P. M., Pauken, K. E., Paley, M. A., Sharpe, A. & Wherry, E. J. Genetic absence of PD-1 promotes accumulation of terminally differentiated exhausted CD8 + T cells. *J Exp Med* **212**, 1125–1137, doi:10.1084/jem.20142237 (2015).
116. Elmore, S. Apoptosis: a review of programmed cell death. *Toxicol Pathol* **35**, 495–516, doi:10.1080/01926230701320337 (2007).
117. Masroori, N., Merindol, N. & Berthoux, L. The interferon-induced antiviral protein PML (TRIM19) promotes the restriction and transcriptional silencing of lentiviruses in a context-specific, isoform-specific fashion. *Retrovirology* **13**, 19, doi:10.1186/s12977-016-0253-1 (2016).
118. Nakahara, F., Weiss, C. N. & Ito, K. The role of PML in hematopoietic and leukemic stem cell maintenance. *Int J Hematol* **100**, 18–26, doi:10.1007/s12185-014-1518-x (2014).
119. Lu, H. *et al.* AFF1 is a ubiquitous P-TEFb partner to enable Tat extraction of P-TEFb from 7SK snRNP and formation of SECs for HIV transactivation. *Proc Natl Acad Sci U S A* **111**, E15-24, doi:10.1073/pnas.1318503111 (2014).
120. Ramakrishnan, R. *et al.* Making a Short Story Long: Regulation of P-TEFb and HIV-1 Transcriptional Elongation in CD4 + T Lymphocytes and Macrophages. *Biology (Basel)* **1**, 94–115,

- doi:10.3390/biology1010094 (2012).
121. Shimazu, T. *et al.* Suppression of oxidative stress by beta-hydroxybutyrate, an endogenous histone deacetylase inhibitor. *Science* **339**, 211–214, doi:10.1126/science.1227166 (2013).
 122. Hird, F. J. & Symons, R. H. The mechanism of ketone-body formation from butyrate in rat liver. *Biochem J* **84**, 212–216, doi:10.1042/bj0840212 (1962).
 123. Hickson, L. J. *et al.* Senolytics decrease senescent cells in humans: Preliminary report from a clinical trial of Dasatinib plus Quercetin in individuals with diabetic kidney disease. *EBioMedicine* **47**, 446–456, doi:10.1016/j.ebiom.2019.08.069 (2019).
 124. Xu, M. *et al.* Senolytics improve physical function and increase lifespan in old age. *Nat Med* **24**, 1246–1256, doi:10.1038/s41591-018-0092-9 (2018).
 125. Jiao, S. *et al.* Differences in Tumor Microenvironment Dictate T Helper Lineage Polarization and Response to Immune Checkpoint Therapy. *Cell* **179**, 1177–1190 e1113, doi:10.1016/j.cell.2019.10.029 (2019).
 126. Mariathasan, S. *et al.* TGFbeta attenuates tumour response to PD-L1 blockade by contributing to exclusion of T cells. *Nature* **554**, 544–548, doi:10.1038/nature25501 (2018).
 127. Watson, D. C. *et al.* Treatment with native heterodimeric IL-15 increases cytotoxic lymphocytes and reduces SHIV RNA in lymph nodes. *PLoS Pathog* **14**, e1006902, doi:10.1371/journal.ppat.1006902 (2018).
 128. R: A language and environment for statistical computing (R Foundation for Statistical Computing, Vienna, Austria, 2018).
 129. Gentleman, R. C. *et al.* Bioconductor: open software development for computational biology and bioinformatics. *Genome Biol* **5**, R80, doi:10.1186/gb-2004-5-10-r80 (2004).
 130. Gentleman, R. *Bioinformatics and computational biology solutions using R and Bioconductor.* (Springer Science + Business Media, 2005).
 131. Benjamini, Y. & Hochberg, Y. Controlling the False Discovery Rate: A Practical and Powerful Approach to Multiple Testing. *Journal of the Royal Statistical Society. Series B (Methodological)* **57**, 289–300 (1995).
 132. Tibshirani, R., Hastie, T., Narasimhan, B. & Chu, G. Diagnosis of multiple cancer types by shrunken centroids of gene expression. *Proc Natl Acad Sci U S A* **99**, 6567–6572, doi:10.1073/pnas.082099299 (2002).
 133. Abdel-Mohsen, M. *et al.* Select host restriction factors are associated with HIV persistence during antiretroviral therapy. *AIDS* **29**, 411–420, doi:10.1097/QAD.0000000000000572 (2015).
 134. Rusinova, I. *et al.* Interferome v2.0: an updated database of annotated interferon-regulated genes. *Nucleic Acids Res* **41**, D1040-1046, doi:10.1093/nar/gks1215 (2013).
 135. Warde-Farley, D. *et al.* The GeneMANIA prediction server: biological network integration for gene prioritization and predicting gene function. *Nucleic Acids Res* **38**, W214-220, doi:10.1093/nar/gkq537 (2010).
 136. Lachmann, A. *et al.* ChEA: transcription factor regulation inferred from integrating genome-wide CHIP-X experiments. *Bioinformatics* **26**, 2438–2444, doi:10.1093/bioinformatics/btq466 (2010).

Figures

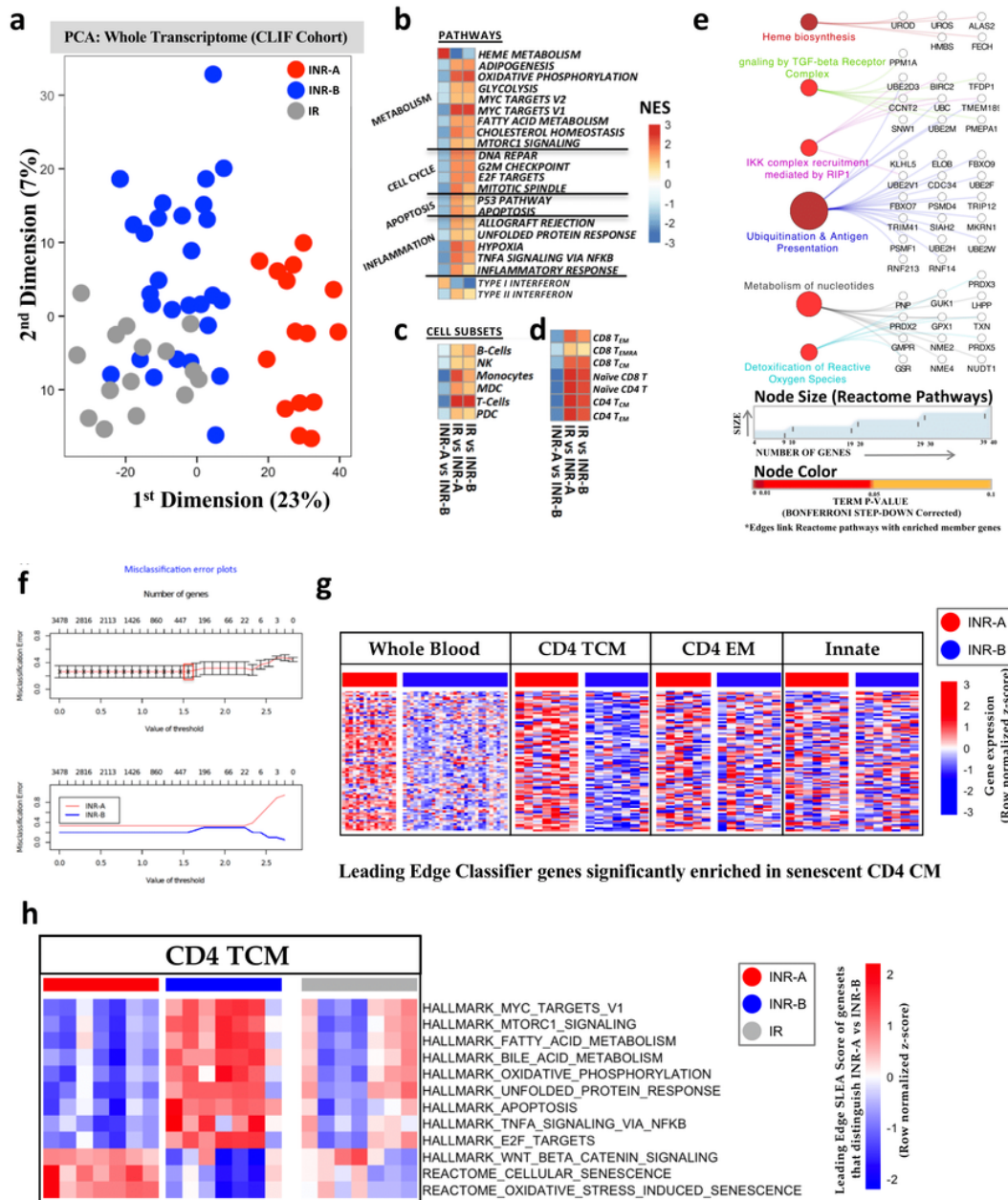


Fig. 1

Figure 1

Whole blood and CD4 subset transcriptional profiling identifies ART-treated Senescent-INRs. a, Multi-dimensional scaling (MDS) was used to reduce the Euclidean distance between whole blood samples of the CLIF cohort (n=61) into two dimensions that summarize the largest transcriptomic variation in the dataset. These two dimensions were used to represent the differences between samples (circles) in the scatter plot. Three groups were identified: IR (Grey; n=17), INR-A (Red; n=14), and INR-B (Blue, n=20). The first dimension of the plot, representing 23% of the transcriptomic variance between samples, depicts the observed transcriptomic difference between the three groups of subjects. b-d, Heatmaps illustrating the normalized enrichment score

(NES; red (high) to blue (low) scale shown on the heatmap) of the top genesets (GSEA p-value ≤ 0.05) MSigDB: Hallmark28 (Table S6) + Interferome Type1/II134 Pathways (b) Major immune cell Subsets34 (Table S7) (c) and T cell subsets35 (Table S8) (d) between IR vs INR-A, IR vs INR-B and INR-A vs INR-B subjects. Each row depicts a genesets, and columns represent the contrast between subject groups. e, Network highlighting the top biological functions associated with genes upregulated in INR-A subjects (vs IRs and INR-Bs; FDR < 0.05). As indicated, node color (dark red to orange) highlights the p-value resulting from over representation analyses, while the node size represents the number of genes per gene-set. Member genes are represented as white circles and connected to member geneset by grey edges (see Table S10 for details). Reactome database was used to annotate the biological functions and the network was plotted using the ClueGo plug-in within cytoscape. f, Training of the 352-gene classifier on the CLIF cohort. Results of the 10-fold cross validation. Misclassification Error plot represents the optimal number of features (genes) that corresponds to the lowest misclassification error rate. The pamr package in R was used to train the classifier via the nearest shrunken centroid method; 352 genes were selected to segregate the two groups of immune non-responders (See Table S11 for list of classifier genes). g, Leading edge genes derived from the 352 gene-based classifier are significantly enriched and segregate Senescent INR subjects in (f) whole blood and (g) sorted CD4 CM cells. Rows represent the z-score normalized genes in the leading edge and columns represent samples of the CLIF cohort: Senescent-INR (Green), and INR-B (Red). h, Heatmap demonstrating the expression of metabolic and senescent specific pathways in CD4 sorted CM cells. Leading-edge genes from the metabolic and senescent pathways identified in prior analyses were summarized into a SLEA representation (z-score per pathway per sample). Rows represent senescent-specific pathways and columns represent samples of the CLIF cohort: IR (Grey), INR-A (Red), and INR-B (Blue). A red-white-blue gradient is used to depict the relative SLEA score of the features, where blue represent a low relative-expression and red a high relative-expression of the feature.

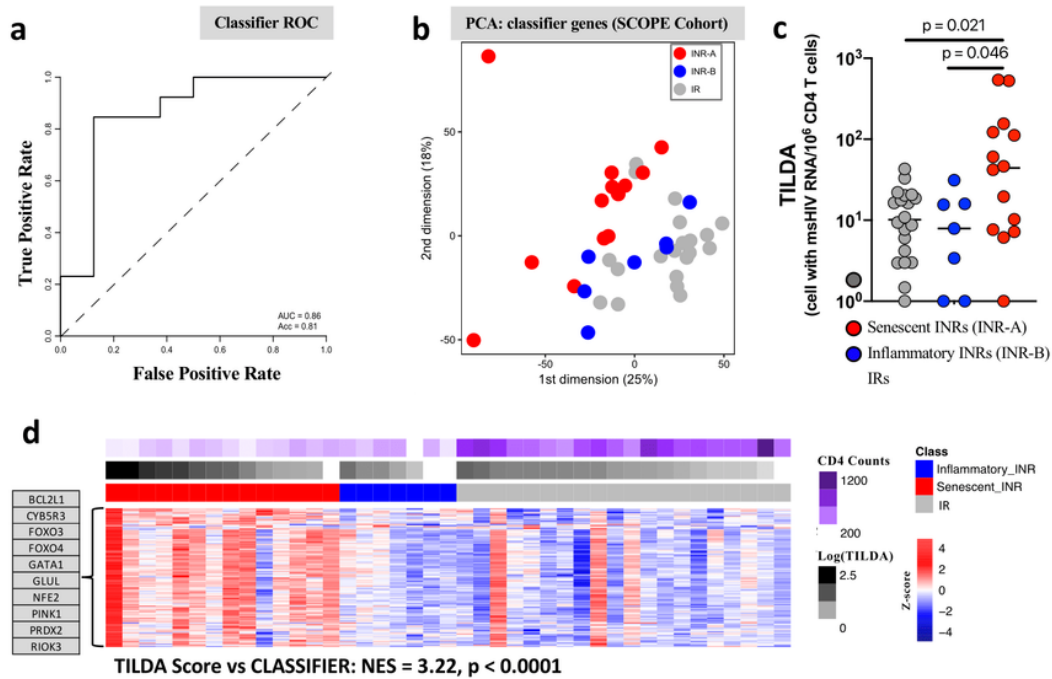


Fig. 2

Figure 2

A 352-geneset signature discriminates ART-treated Senescent-INRs and is associated with high inducible HIV. a, Receiver operating characteristics (ROC) curve for the genes as predictors of INR groups. X- and Y- axes represent the False and True positive rates of prediction on the SCOPE validation dataset. A 352 gene-based classifier (see Table S11 for list of genes) trained on the CLIF cohort segregates INR-A and INR-B subjects in the SCOPE cohort with an accuracy of 81%. The classifier which was tested across different microarray platforms confirmed the heterogeneity of ART-treated INR subjects in these two independent cohorts (see methods for details on approach used to build the classifier). b, Multi-dimensional Scaling was used to summarize the

variation of the 352 genes of the classifier among subjects of the SCOPE cohort (n=41). Senescent-ISR (Red), and ISR-B (Blue) were identified along the first dimension of the MDS plot. c, Jitter plot illustrates significantly (Wilcoxon rank test p-values shown on plot) higher levels of inducible HIV (measured by TILDA73) in Senescent-ISRs compared to ISRs and ISR-Bs. d, Heatmap illustrating the leading edge from the gene-based classifier that predict inducible HIV among subjects of the SCOPE cohort (n = 41; linear regression: classifier genes ~ inducible HIV, GSEA: NES=3.22, p<0.0001). Rows represent the z-score normalized genes in the leading edge and columns represent samples of the SCOPE cohort: ISR (Grey), Senescent-ISR (Red), and ISR-B (Blue). As indicated in the legend, each row is z-score normalized. The magnitude of CD4 counts (purple) and the size of inducible HIV (black) are plotted as annotations at the top of the heatmap, as indicated. Selected genes are highlighted in boxes to the left of the heatmap (See Table S12 for full leading-edge gene list).

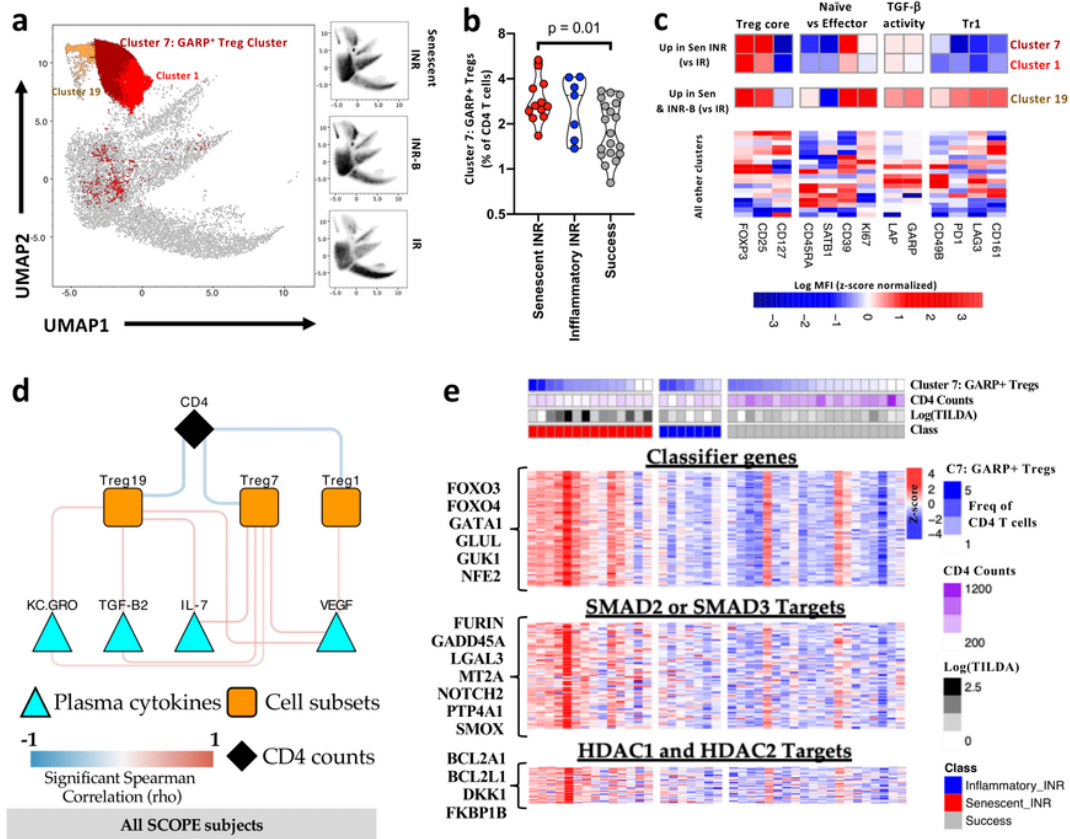


Fig. 3

Figure 3

TGF-β signaling cascade exemplified by an increase in SMAD2/3 targets and an increase in TGF-β producing Tregs is associated with an increase in inducible HIV and drives latent HIV in vitro. a, Treg panel clusters determined using the PhenoGraph method (see Table S14) and visualized using the Uniform Manifold Approximation and Projection (UMAP) analysis were used to represent the distribution of Treg phenotypes in total CD4 T cells (using high-dimensional flow cytometry) in IR, Senescent-INR, and INR-B subjects of the SCOPE cohort. FOXP3 expressing clusters that were abundant in Senescent-INR subjects (vs IRs) are highlighted on the UMAP plot (See Table S14 for details). b, Violin plot illustrates significantly higher

frequencies of Treg cluster 7 (in total CD4 T-cells) in Senescent INR subjects. Wilcoxon rank test was used to assess significance and p-values are indicated on the plot. c, Heatmap highlighting the differences in markers between clusters. FOXP3+ clusters that were abundant in senescent INRs (i.e. clusters 1,7, and 19) are highlighted. Each column is z-score normalized value of the mean fluorescence intensity (raw intensities for every cluster can be found in Table S14). d, Network highlighting a positive correlation between FOXP3 expressing Treg clusters that are abundant in Senescent INRs (Clusters 1, 7 and 19) with plasma cytokine levels (of cytokines in cytokine cluster 3; See Supplementary Fig. 4b) measured on the same subjects. Triangular blue nodes depict plasma cytokines IL-7, TGF- β 2, KC.GRO and VEGF; red edges highlight a positive correlation between those cytokines and the Treg clusters. Orange squares reflect high-density flow cytometry clusters, light blue triangles reflect plasma cytokine levels, red edges indicate significant positive correlation. A Spearman correlation test was used to assess significance (p-value <0.05) across IR, Senescent-INR, and INR-B subjects of the SCOPE cohort (Table S16 lists the details of correlations between plasma cytokine cluster 3 members and Treg subsets). e, Heatmap highlighting overlapping leading-edge genes from the association of inducible HIV and frequencies of Treg cluster 7 with the 352 gene-based classifier genes (top block), SMAD2/3 targets (middle block) and HDAC1/2 targets (bottom block). Rows represent features and columns represent samples of the SCOPE cohort: IR (Grey), INR-A (Red), and INR-B (Blue). The gene-expression per row was centered at zero and to a standard deviation of 1 (z-score). As indicated in the figure, a red-white-blue gradient is used to depict the relative expression of the features. The magnitude of CD4 counts (purple), frequencies of Treg Cluster7 (GARP+, dark blue) and size of HIV inducible reservoir (black) are plotted as annotations at the top of the heatmap. GSEA was used to assess the association between the features and inducible HIV/Treg cluster 7 frequencies (linear regression, p<0.05). Genes that showed a significant overlap (GSEA vs inducible HIV and Treg cluster 7 frequencies; significance (p-value <0.05 - assessed by Fischer exact test) amongst the leading-edge gene list/pathway are represented on the heatmap (See Table S17 for all the details).

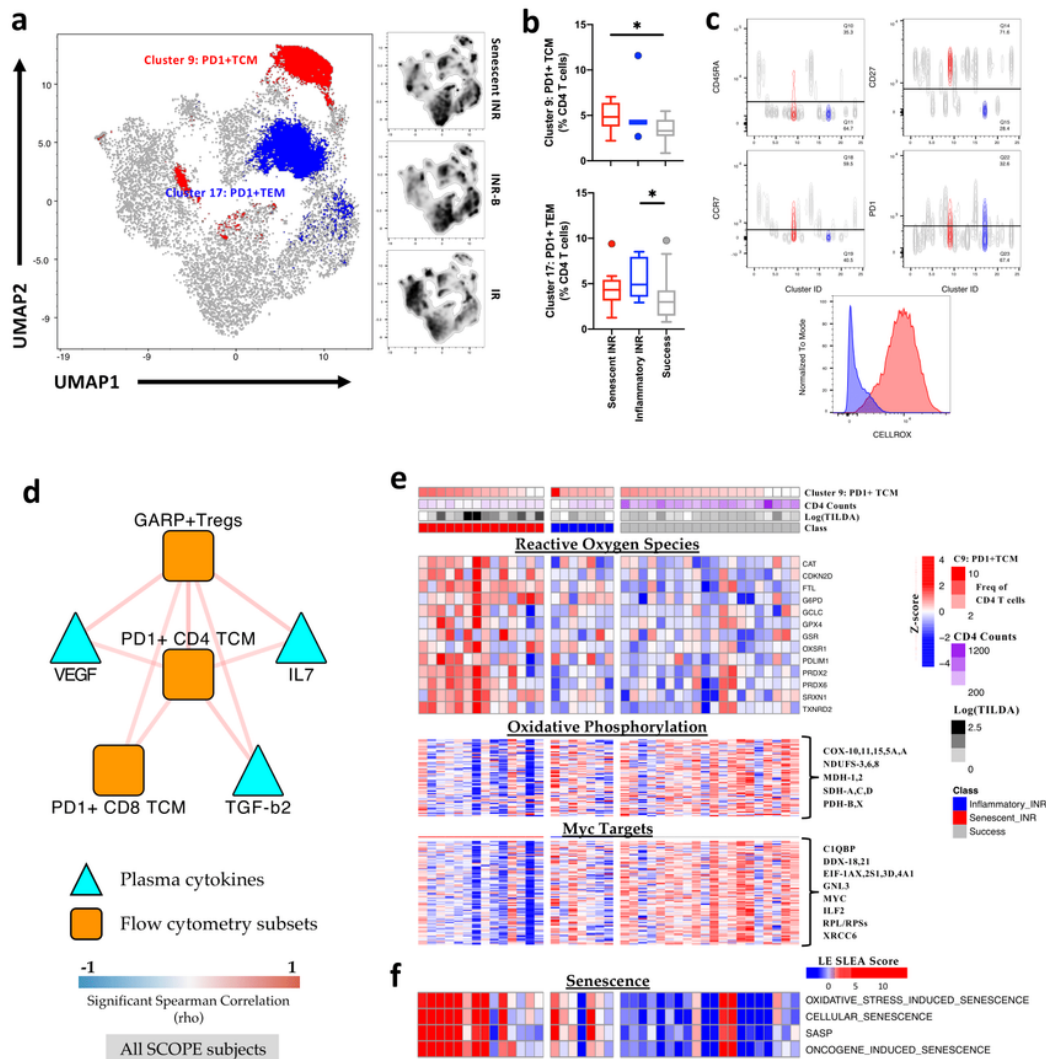


Fig. 4

Figure 4

Heightened frequencies of PD1hiROShi CD4 TCMs and lower CD4 counts in Senescent INRs are associated with poor mitochondrial metabolism and senescence. a, Clusters determined using the PhenoGraph method and visualized using the Uniform Manifold Approximation and Projection (UMAP) analysis were used to represent the distribution of CD4 T cells subsets, surface expression of PD-1 and markers of mitochondrial activity in CD4 T cells (using high-dimensional flow cytometry) in IR, Senescent-INR, and INR-B subjects of the SCOPE cohort (See Table S18 for details). Density Plots highlight the enrichment of a specific cluster “Cluster 9: PD1+TCM” in Senescent-INR subjects. b, Box plots illustrate unique and significantly higher frequencies of

Cluster 9 (PD1+TCM in total CD4 T-cells) in Senescent INR subjects and Cluster 17 (PD1+TEM in total CD4 T cells) in the Inflammatory INR. A Wilcoxon rank test was used to assess significance (*p-value of <0.05) (Table S18). c, MFIs of cell surface (CD45RA, CD27, CCR7, PD1) per cluster are shown. Clusters 9 (red) and 17 (blue) are overlaid to highlight the heightened levels of CD27 and CCR7 in Cluster 9 (i.e. TCM), and low levels of CD27 and CCR7 in Cluster 17 (i.e. TEM). Both clusters showed relatively low levels of CD45RA and high levels of PD1. Black line across each plot discriminated traditionally gated negative population from the its positive counterpart. A head-to-head comparison between clusters 9 and 17 revealed a distinct upregulation in CellROX within cluster 9 (i.e. PD1+ TCMs that are increased in the senescent INRs) (Raw MFIs of all clusters are listed in Table S18). d, Correlation network highlighting significant associations between PD1+TCM cluster frequencies and plasma cytokine in the pool of Senescent INRs and IRs (i.e. driven by lower CD4 counts in Senescent INRs vs IRs). Triangular blue nodes depict plasma cytokines; orange squares reflect high-density flow cytometry clusters; and red edges highlight a positive correlation between cytokines and cell clusters. A Spearman correlation test was used to assess significance (all edges have a significant p-value <0.05) across IR and Senescent-INR subjects of the SCOPE cohort. e, Heatmap highlighting a positive association between Reactive Oxygen Species and CD4 numbers (top block) and a negative association between Oxphos/targets of Myc and CD4 numbers (middle and bottom blocks) respectively. GSEA was used to assess the association between the features and CD4 numbers/PD1+ TCM frequencies (linear regression, p<0.05). Genes that showed a significant overlap (GSEA vs inducible HIV and PD1+ TCM frequencies; significance (p-value <0.05) assessed by Fischer exact test) amongst the leading-edge gene list/pathway are represented in the heatmap (See Table S20 for overlapping gene-lists and leading-edge gene lists). Rows represent z-score normalized (red-white-blue gradient) genes and columns represent subjects from the SCOPE cohort: IR (Grey), INR-A (Red), and INR-B (Blue). The magnitude of CD4 counts (purple), frequencies of PD1+TCM (dark red) and inducible HIV (black) are plotted as annotations at the top of the heatmap. f, Heatmap demonstrating the association of senescent specific pathways PD1+TCM cluster. Leading-edge genes from the association of PD1+TCM and senescence pathway were summarized into a SLEA representation (z-score per pathway per sample) (See Table S20 for details). Rows represent senescent-specific pathways and columns represent samples of the SCOPE cohort: IR (Grey), INR-A (Red), and INR-B (Blue). A red-white-blue gradient is used to depict the relative SLEA score of the features, where blue represent a low relative-expression and red a high relative-expression of the feature. The magnitude of CD4 counts (purple), frequencies of PD1+TCM (dark red) and inducible HIV (black) are plotted as annotations at the top of the heatmap.

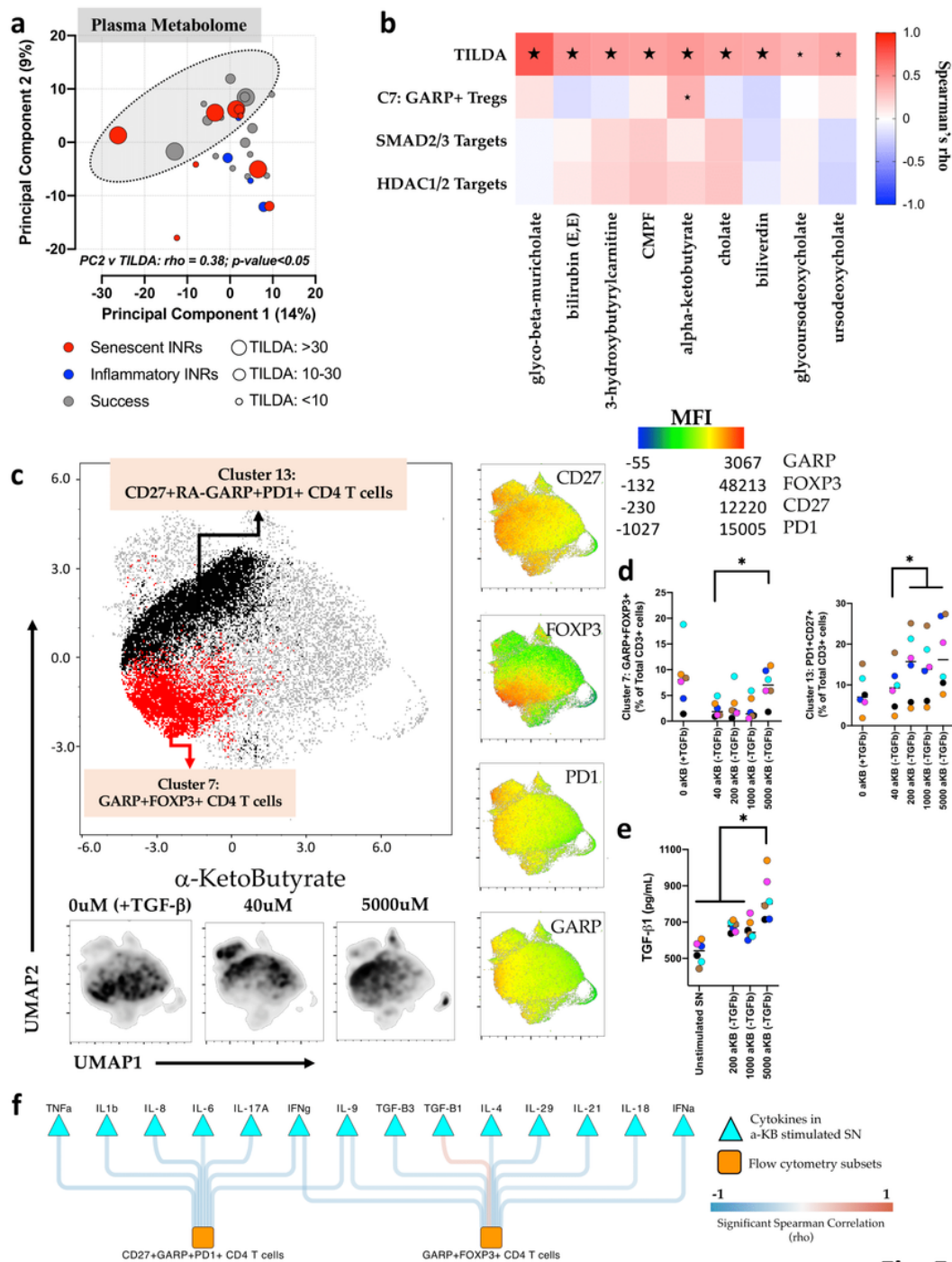


Fig. 5

Figure 5

Ex vivo plasma bile acid/hydroxybutyrate levels and in vitro α -ketobutyrate stimulation drives the differentiation TGF- β producing Tregs. a, Principal Component Analysis of all plasma metabolome highlights a cluster of subjects with high TILDA levels and reveals a significant negative correlation between PC1 (x-axis) and the Classifier gene-set and a significant positive correlation between PC2 (y-axis) and TILDA. Spearman Correlation was used to assess significance, ρ and p -values provided on the figure. b, Correlation matrix heatmap between abundance of plasma bile acid/microbial metabolites (plotted along the y-axis) and variables of interest including TILDA levels, GARP+ Tregs, SMAD2/3 and HDAC1/2 Targets (plotted along the y-

axis). Analysis highlights α -ketobutyrate as the metabolite correlated with levels of TILDA and GARP+ Tregs. A Spearman correlation was used to assess significance. Stars on the heatmap highlight significant correlations ($P < 0.05$: large star, $P < 0.1$: small star). c, in-vitro experiment to assess the impact of increasing concentrations of α -ketobutyrate on sorted naïve CD4 T cells from healthy subjects in the presence of IL-2, anti-CD3/28 antibodies and/or TGF- β . Dimension Reduction of high density flow cytometry analysis highlights UMAP1 and UMAP2 on X- and Y- axes respectively and illustrates that stimulation in the presence of TGF- β led to a profound increase in frequencies of GARP+FOXP3+ cells (a, Cluster 7) and GARP+PD1+ cells (a, Cluster 13). d Jitter plots highlighting that increasing concentrations of α -ketobutyrate preferentially led to differentiation into GARP+FOXP3+ cells and increased levels of PD1 expressing quiescent cells. GARP+FOXP3+ and PD1+CD27+ levels plotted along the Y-axis, while α -ketobutyrate increasing concentration levels are indicated on the X-axis. Conditions in the absence of TGF- β are designated with (-TGF- β). A Mann-Whitney U-test was used to assess significance across concentrations (* represents p-value < 0.05 between groups). e, Plasma cytokine levels of TGF- β 1 significantly increase with enhanced α -ketobutyrate stimulation. TGF- β 1 levels plotted along the Y-axis, while α -ketobutyrate concentration levels are indicated on the X-axis. A Mann-Whitney U-test was used to assess significance across concentrations (* represents p-value < 0.05 between groups). f, CD4 T cell subsets enriched after stimulation with α -ketobutyrate (i.e. GARP+ Tregs and PD1+ TCM; nodes in orange squares), were significantly positively associated ($p < 0.05$; Spearman's $\rho > 0$ - red edges) with an increase in secreted TGF- β 1 and a significant decrease in effector cytokines like IL17A, IFN γ and IL9 ($p < 0.05$; Spearman's $\rho < 0$ - blue edges).

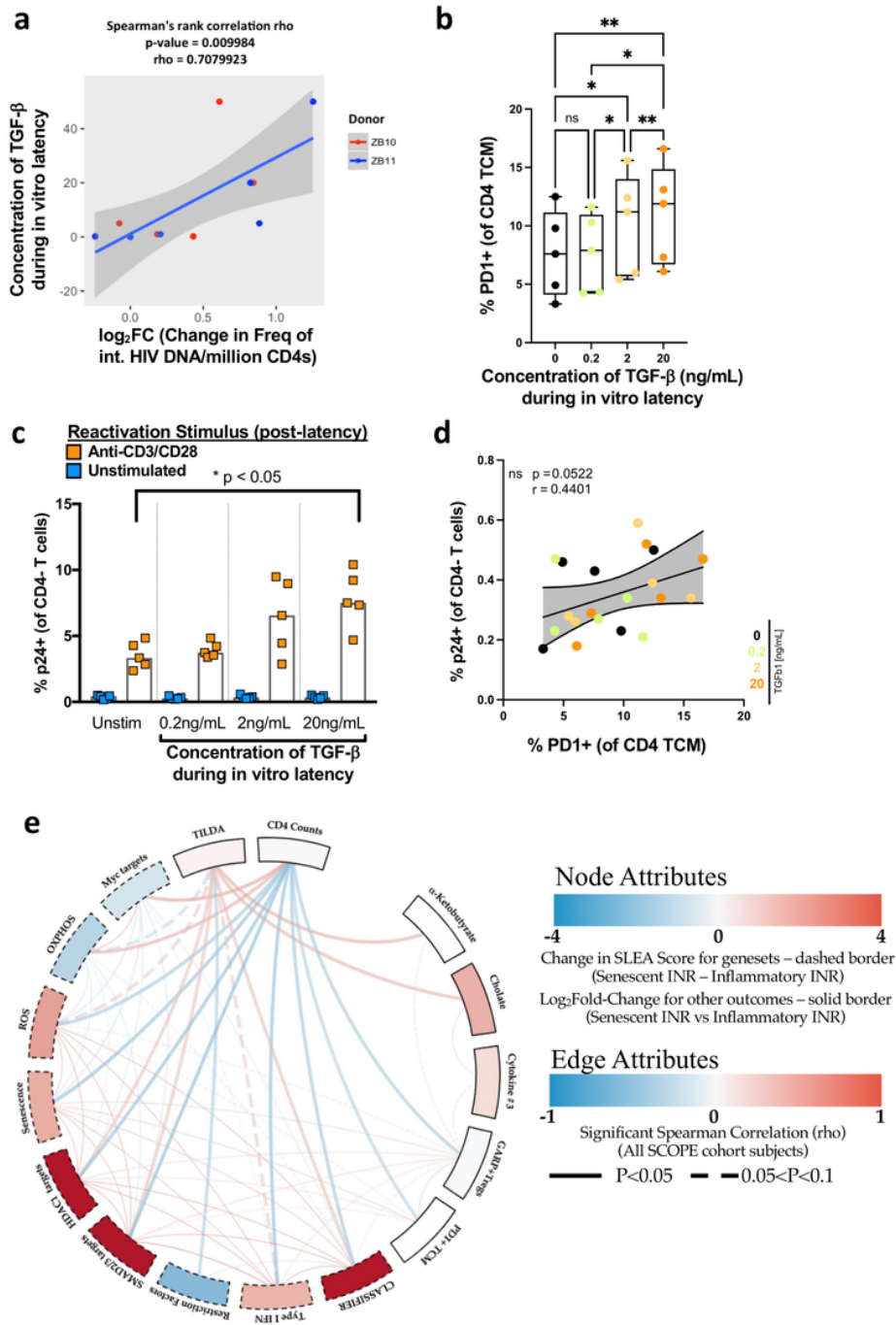


Fig. 6

Figure 6

TGF- β levels define PD-1 surface protein expression and frequencies of CD4 T cells with latent HIV in vitro. a-d, LARA assay in vitro model was used to characterize the impact of dose-dependent increased in TGF- β on the establishment of HIV latency in memory CD4+ T cells. Increasing concentrations of TGF- β (0.2-20ng/mL) during LARA latency culture results in heightened frequencies of CD4 T cells with integrated HIV DNA (a) and higher surface protein levels of PD1 in the CD4 TCM compartment (b). The activation of latent CD4 T cells using anti-CD3/28 antibodies stimulation resulted in an increase in the frequencies of p24+ CD4 T cells (c). Higher frequencies of p24+ CD4 T cells were significantly associated with frequencies of PD-1+ CD4 TCMs (d).

A Mann-Whitney U-test was used to assess significance across concentrations (* represents p-value <0.05 between groups). A Spearman correlation test was used to assess significance for all correlations. (e) Circle plot highlighting an integrated model associating leading/overlapping edges from genesets identified (classifier gene-set and biological pathways) in Figs 1 to 4, GARP+ Treg frequencies (grey), and PD1+TCM frequencies (grey) and with outcomes (CD4 counts, TILDA inducible HIV (orange)) across SCOPE cohort (n = 41). SLEA scores (z-score per pathway per sample) were calculated for each of these gene-lists (see Table S20 for the scores) and spearman's test was used to assess correlation between all of the features mentioned. Color gradient of the Pathway node (white to red, white to blue) reflects relative enrichment (positive or negative; respectively) of pathway in Senescent-INRs compared to IR subjects. Edges between nodes represent a significant positive or negative correlation (red or blue respectively) (details for the full network are summarized in Table S20).

Supplementary Files

This is a list of supplementary files associated with this preprint. Click to download.

- [IRINRSupplementaryTablesSep2021ForNIsubmission.pdf](#)
- [SupplementaryFigureLegends.docx](#)